

# The effect of phase change on stability of convective flow in a layer of volatile liquid driven by a horizontal temperature gradient

Roman O. Grigoriev, Tongran Qin

School of Physics, Georgia Institute of Technology, Atlanta, GA 30332-0430, USA

(Received 5 April 2017)

Buoyancy-thermocapillary convection in a layer of volatile liquid driven by a horizontal temperature gradient has been studied extensively in experiment and numerics. Recent studies have shown that the composition of the gas phase, which is typically a mixture of vapour and air, has a noticeable effect on the critical Marangoni number describing the onset of convection as well as on the observed convection pattern. Specifically, as the total pressure or, equivalently, the average concentration of air is decreased, the threshold of the instability leading to the emergence of convective rolls is found to increase rather significantly. We present a linear stability analysis of the problem which shows that this trend can be readily understood by considering the transport of heat and vapour through the gas phase. In particular, we show that transport in the gas phase has a noticeable effect even at atmospheric conditions, when phase change is greatly suppressed.

## 1. Introduction

Convection in fluids with a free surface driven by a horizontal temperature gradient has been studied extensively due to applications in crystal growth and thermal management. The first systematic study of convection in nonvolatile fluids appears to be due to Birikh (1966) who derived an analytic solution for a planar return flow in a laterally unbounded layer due to both buoyancy and thermocapillary stresses. This solution also describes the flow away from the end walls in a laterally bounded geometry: thermocapillary stresses drive the flow from the hot end towards the cold end near the free surface, with a return flow near the bottom of the layer. Kirdyashkin (1984) repeated Birikh's theoretical analysis and validated the analytical solutions experimentally.

Smith & Davis (1983 $a,b$ ) performed a linear stability analysis of such flows in the limit of vanishing dynamic Bond number,  $Bo_D$  (i.e., ignoring buoyancy effects). They predicted that, depending on the Prandtl number of the liquid, the uniform base flow would undergo an instability towards either surface waves (for  $Pr < 0.15$ , which corresponds to liquid metals) or hydrothermal waves (for  $Pr > 0.15$ , which corresponds to gases and non-metallic liquids) above a critical Marangoni number  $Ma$ , which characterizes the magnitude of thermocapillary stresses. In particular, hydrothermal waves were predicted to form at an angle to the direction of the thermal gradient and travel in the direction of thermal gradient. As  $Pr$  increases, the angle changes smoothly from nearly transverse to nearly parallel to the thermal gradient. The theoretical predictions have since been thoroughly tested and verified both in microgravity and for thin films in terrestrial conditions. A thorough overview of these experiments is presented in a review paper by Schatz & Neitzel (2001).

A different type of instability is found at  $Bo_D = O(1)$ , when buoyancy is non-negligible. Villers & Platten (1992) studied buoyancy-thermocapillary convection in a rectangular

cavity for acetone ( $Pr = 4.24$ ) experimentally and numerically. Although acetone is volatile, reasonable agreement was found between the experimental observations at atmospheric conditions and the numerical simulations based on a one-sided model that ignored heat and mass transfer in the gas phase. For low  $Ma$  a featureless planar return flow was found, which is well-described by Birikh's solution. At higher  $Ma$  a steady cellular pattern featuring multiple convection rolls was found instead of hydrothermal waves. The (transverse) convection rolls were found to rotate in the same direction, unlike the case of pure buoyancy (or Rayleigh-Bénard) convection driven by a vertical temperature gradient. At even higher  $Ma$  the steady state was found to be replaced by an oscillatory pattern that was also unlike a hydrothermal wave: the convection rolls were observed to travel in the direction opposite to that of the thermal gradient. Similar results were obtained later by De Saedeleer *et al.* (1996) for decane ( $Pr = 15$ ) and Garcimartín *et al.* (1997) for 0.65 cSt and 2.0 cSt silicone oil ( $Pr = 10$  and 30, respectively) in rectangular cavities with strong confinement in the spanwise direction.

Riley & Neitzel (1998) performed one of the most extensive and detailed experimental studies of convection in 1 cSt silicone oil ( $Pr = 13.9$ ) in a rectangular cavity with a spanwise dimension comparable to the streamwise dimension. They discovered that a direct transitions from steady, unicellular flow to hydrothermal waves takes place for small values of the dynamic Bond number ( $Bo_D \lesssim 0.2$ ), while for  $Bo_D \gtrsim 0.2$  the results are similar to those of earlier studies with spanwise confinement: the featureless return flow first transitions to steady co-rotating convection cells and, upon further increase in  $Ma$ , to an oscillatory multicellular pattern. Riley and Neitzel also determined the critical values of  $Ma$  and the wavelength  $\lambda$  of the convective pattern as a function of  $Bo_D$ . Burguete *et al.* (2001) performed experiments on convection in 0.65 cSt silicone oil ( $Pr = 10.3$ ) in a rectangular cavity with different aspect ratios where spanwise dimension was greater than the streamwise dimension. Similarly, they found that the base return flow destabilizes into either oblique travelling waves or longitudinal stationary rolls, respectively, for small and large thickness of the liquid layer (i.e., low and high  $Bo_D$ ).

Convective patterns have also been studied using numerical simulations. Most of the numerical studies (Villers & Platten 1992; Ben Hadid & Roux 1992; Mundrane & Zebib 1994; Lu & Zhuang 1998; Shevtsova *et al.* 2003) were based on one-sided models which ignore the transport in the gas phase, assume that the free surface is flat and non-deformable, the bottom wall and the interface are adiabatic, and phase change is negligible. These numerical simulations were able to reproduce some features of the experimental studies. For example, Shevtsova *et al.* (2003) and Shevtsova & Legros (2003) performed numerical simulations for decane ( $Pr = 14.8$ ) in a rectangular layer at different  $Bo_D$ . They found that as  $Ma$  increases, the primary instability leads to hydrothermal waves for  $Bo_D \leq 0.25$ , while for  $Bo_D \geq 0.32$  the primary (secondary) instability produces a steady (oscillatory) multicellular flow.

Since it does not account for buoyancy, the linear stability analysis of Smith & Davis (1983*a,b*) fails to predict the stationary patterns that emerge for  $Bo_D = O(1)$ . However, most of the linear stability analyses accounting for buoyancy also failed to predict the correct pattern, i.e., stationary (transverse) multicells that were observed in the experiments. Using adiabatic boundary conditions at the top and bottom of the liquid layer, Parmentier *et al.* (1993) predicted transition to travelling waves rather than steady multicellular pattern for a range of  $Pr$  from 0.01 to 10, regardless of the value of  $Bo_D$ . Chan & Chen (2010), who used similar assumptions, also predicted transition to travelling waves for a  $Pr = 13.9$  fluid. Moreover, their predicted critical  $Ma$  and wavelength  $\lambda$  do not match the experiment (Riley & Neitzel 1998). In both cases the predicted travelling

waves are oblique for smaller  $Bo_D$  and become transverse for  $Bo_D$  greater than some critical  $O(1)$  value.

Mercier & Normand (1996) showed that transition to a stationary convective pattern can take place if the adiabatic boundary conditions are replaced with Newton's cooling law, although that requires an unrealistically large surface Biot number ( $Bi \gtrsim 185/Bo_D$ ). Moreover, the predicted pattern corresponds to longitudinal convection rolls, while in most experiments transverse rolls were observed. In a subsequent paper Mercier & Normand (2002) considered the effects of the end walls, which they described as spatial disturbances superimposed on the uniform base flow. Their analysis predicted that, depending upon the Prandtl number, convection rolls would develop near the hot end (for  $Pr > 4$ ), near the cold end (for  $Pr < 0.01$ ) or at both end walls (for  $0.01 < Pr < 4$ ).

To our knowledge, the study by Priede & Gerbeth (1997) is the only one to date which correctly predicts the formation of a stationary pattern at  $Bo_D = O(1)$ . They argued that travelling waves, being convectively unstable, cannot get sufficiently amplified by linear instability in a laterally bounded system. At the same time, the lateral walls induce a disturbance with relatively large amplitude, which penetrates into the bulk of the liquid layer, as the base flow becomes unstable with respect to a stationary pattern of transverse convection rolls. Their predicted critical values of  $Ma$  are in reasonable agreement with the threshold values found by Riley & Neitzel (1998), although the analytical prediction systematically overestimates the critical  $Ma$ , suggesting that some important effects have not been considered.

The volatility of the fluids used in the experiments is one source of the discrepancy with analytical (and most numerical) predictions. Although at atmospheric conditions phase change is usually strongly suppressed, it can still play a role. The latent heat associated with phase change can significantly modify the interfacial temperature, and hence the thermocapillary stresses. However, there are very few studies that investigated this effect. Li *et al.* (2012) have studied non-adiabatic effects by using Newton's cooling law with a small Biot number. Their numerical simulations ignored phase change, but were able to reproduce many features of the experimental observations at atmospheric conditions. Ji *et al.* (2008) considered phase change, but ignored buoyancy, so their analysis is only applicable for thin films or under microgravity when  $Bo_D \approx 0$ .

A few recent studies investigated the role played by the gas phase, which is generally a binary mixture of a noncondensable gas (typically air) and the vapour, in more detail. In particular, the experimental study of Li *et al.* (2014), which used volatile 0.65 cSt silicone oil ( $Pr = 9.2$ ), showed that the threshold values of  $Ma$  increase rather dramatically as the air is removed from the experimental apparatus. The numerical simulations of this experimental setup (Qin *et al.* 2014, 2015; Qin & Grigoriev 2015) based on a two-sided model, which took phase change into account and explicitly described the transport of heat and vapours through the gas phase, reproduced the experimental results. The main effect of air is to suppress phase change by impeding the transport of vapour towards, or away from, the interface, but its presence also affects thermal conductivity of the gas layer. This suggests that phase change and transport in the gas phase play an important role in this problem, especially at reduced pressures (reduced concentrations of air).

In order to better understand the mechanism of the instability and the effect of the gas phase we performed a linear stability analysis of the two-sided model of the flow, which is described in Section 2. The analytical solutions describing the uniform return flow (in both phases) is derived in Section 3. The stability of that solution is investigated in Section 4. The results of linear stability analysis are compared with existing experimental and numerical studies in Section 5 and are discussed in Section 6. Conclusions are presented in Section 7.

## 2. Mathematical Model

### 2.1. Governing Equations

We will assume that the liquid layer is flat and has a depth  $d_l$  and lateral dimensions much larger than  $d_l$ . Since in most experiments the system is covered by a horizontal plate to limit evaporation, we will assume that the gas layer also has a finite depth  $d_g$ . To describe convection in this two-layer system, we will use a variation of the two-sided model originally introduced by Qin *et al.* (2014) for near-atmospheric conditions and later extended by Qin & Grigoriev (2015) to the limit when the gas phase is dominated by the vapour, rather than air. A version of the model applicable in both limits is summarized below. The momentum transport in the bulk is described, for both the liquid and the gas phase, by the Navier-Stokes equation

$$\rho(\partial_t \mathbf{u} + \mathbf{u} \cdot \nabla \mathbf{u}) = -\nabla p + \mu \nabla^2 \mathbf{u} + \rho(T, c_a) \mathbf{g} \quad (2.1)$$

where  $p$  is the fluid pressure,  $\rho$  and  $\mu$  are the fluid's density and viscosity, respectively,  $c_a$  is the concentration of air, and  $\mathbf{g}$  is the gravitational acceleration. (The air is non-condensable, so  $c_a = 0$  in the liquid phase.) Following standard practice, we use the Boussinesq approximation, retaining the temperature and composition dependence only in the last term to represent the buoyancy force. In the liquid phase

$$\rho_l = \rho_l^0 [1 - \beta_l (T - T^0)], \quad (2.2)$$

where  $\rho_l^0$  is the reference density at the reference temperature  $T^0$  and  $\beta_l = -\rho_l^{-1} \partial \rho_l / \partial T$  is the coefficient of thermal expansion. Here and below, subscripts  $l$ ,  $g$ ,  $v$ ,  $a$ , and  $i$  denote properties of the liquid and gas phase, vapour and air component, and the liquid-vapour interface, respectively. In the gas phase

$$\rho_g = \rho_a + \rho_v, \quad (2.3)$$

where both vapour and air are considered to be ideal gases

$$p_{a,v} = \rho_{a,v} \bar{R}_{a,v} T, \quad (2.4)$$

$\bar{R}_{a,v} = R/M_{a,v}$ ,  $R$  is the universal gas constant, and  $M_{a,v}$  is the molar mass of air/vapour. On the left-hand-side of (2.1) the density is considered constant for each phase:  $\rho_l = \rho_l^0$  in the liquid and  $\rho_g = \rho_a^0 + \rho_v^0$  in the gas.

The flow in both phases is not, strictly speaking, incompressible due to the variation in the density with temperature and/or composition. The continuity equation in the liquid is

$$\partial_t \rho_l + \nabla \cdot (\rho_l \mathbf{u}) = 0. \quad (2.5)$$

The flows we are interested in change slowly in time, so that

$$\nabla \cdot \mathbf{u} \approx \beta_l \mathbf{u} \cdot \nabla T. \quad (2.6)$$

In the gas phase, the total number density is given by

$$n_g = n_a + n_v = \frac{p_g}{k_B T}, \quad (2.7)$$

where  $n_{a,v} = \rho_{a,v}/m_{a,v}$ ,  $m_{a,v} = M_{a,v}/N_A$  is the mass of one air/vapour molecule,  $k_B = R/N_A$  is the Boltzmann constant,  $N_A$  is the Avogadro number, and

$$p_g = p_a + p_v \quad (2.8)$$

is the total gas pressure.

Mass transport of both air and vapour in the gas phase is described by the advection-diffusion equation for the number (or mass) density

$$\partial_t n_{a,v} + \nabla \cdot \mathbf{j}_{a,v} = 0, \quad (2.9)$$

where we introduced the number density flux

$$\mathbf{j}_{a,v} \equiv n_{a,v} \mathbf{u} - n_g D \nabla c_{a,v} = n_g (\mathbf{u} c_{a,v} - D \nabla c_{a,v}), \quad (2.10)$$

where

$$c_{a,v} \equiv \frac{n_{a,v}}{n_g} = \frac{p_{a,v}}{p_g} \quad (2.11)$$

are the concentrations (or, more precisely, the molar fractions) of the two components in the gas phase. The first term in (2.9) represents advection, the second term represents diffusion, and  $D$  is the binary diffusion coefficient. As we showed previously (Qin *et al.* 2015), spatial variation of  $p_g$  can in practice be neglected, so according to (2.7)  $n_g \propto T^{-1}$ . Hence, for slowly varying flows, we can use the continuity equation for the gas phase

$$\partial_t n_g + \nabla \cdot (n_g \mathbf{u}) = 0, \quad (2.12)$$

which follows directly from (2.9), to find the direct analogue of (2.6):

$$\nabla \cdot \mathbf{u} \approx T^{-1} \mathbf{u} \cdot \nabla T. \quad (2.13)$$

In both phases, the flow can be considered incompressible

$$\nabla \cdot \mathbf{u} \approx 0 \quad (2.14)$$

(and the number density  $n$  constant in each phase) for sufficiently small temperature gradients. The analysis presented below assumes that is the case. Consequently, (2.9) reduces to an equation for the molar fraction

$$\partial_t c_{a,v} + \mathbf{u} \cdot \nabla c_{a,v} = D \nabla^2 c_{a,v}. \quad (2.15)$$

Finally, the transport of heat is also described using an advection-diffusion equation

$$\partial_t T + \mathbf{u} \cdot \nabla T = \alpha \nabla^2 T, \quad (2.16)$$

where  $\alpha = k/(\rho C_p)$  is the thermal diffusivity,  $k$  is the thermal conductivity, and  $C_p$  is the heat capacity, of the fluid.

## 2.2. Boundary Conditions at the Interface

The system of coupled evolution equations for the velocity, pressure, temperature, and number density fields should be solved in a self-consistent manner, subject to the boundary conditions describing the balance of momentum, heat, and mass fluxes. The phase change at the free surface can be described using Kinetic Theory (Schrage 1953). As we have shown previously (Qin *et al.* 2015), the choice of the phase change model has negligible effect on the results. The mass flux across the interface is given by (Klentzman & Ajaev 2009)

$$J = \frac{2\chi}{2-\chi} \rho_v \sqrt{\frac{\bar{R}_v T_i}{2\pi}} \left[ \frac{p_l - p_g}{\rho_l \bar{R}_v T_i} + \frac{\mathcal{L}}{\bar{R}_v T_i} \frac{T_i - T_s}{T_s} \right], \quad (2.17)$$

where  $\chi$  is the accommodation coefficient,  $\mathcal{L}$  is the latent heat, and subscript  $s$  denotes saturation values for the vapour. The dependence of the local saturation temperature on the partial pressure of vapour is described using the Clausius-Clapeyron equation for

phase equilibrium

$$\ln \frac{p_v}{p_v^0} = \frac{\mathcal{L}}{\bar{R}_v} \left[ \frac{1}{T_0} - \frac{1}{T} \right], \quad (2.18)$$

where  $p_v^0$  is the (saturation) pressure at temperature  $T_0$ . The first term in (2.17) is proportional to the Young-Laplace pressure and can be ignored in this problem, since the interface is essentially flat.

The mass flux balance at the interface can be expressed with the help of (2.9). In the reference frame of the interface, the mass flux of the vapour is given by

$$\frac{J}{m_v} = \mathbf{n} \cdot \mathbf{j}_v = n_g \hat{\mathbf{n}} \cdot ([\mathbf{u}_g - \mathbf{u}_i]c_v - D\nabla c_v), \quad (2.19)$$

where  $\mathbf{u}_i$  is the velocity of the liquid at the interface. Since air is noncondensable, its mass flux across the interface is zero:

$$0 = \mathbf{n} \cdot \mathbf{j}_a = n_g \hat{\mathbf{n}} \cdot ([\mathbf{u}_g - \mathbf{u}_i]c_a - D\nabla c_a). \quad (2.20)$$

Since  $c_a + c_v = 1$ , these two relations can be solved yielding two of the boundary conditions for (2.1) and (2.9) in the gas phase

$$\hat{\mathbf{n}} \cdot \nabla c_v = -\frac{c_a J}{m_v n_g D} \quad (2.21)$$

and

$$\hat{\mathbf{n}} \cdot (\mathbf{u}_g - \mathbf{u}_i) = \frac{J}{m_v n_g}. \quad (2.22)$$

The heat flux balance is given by

$$\mathcal{L}J = \hat{\mathbf{n}} \cdot k_g \nabla T_g - \hat{\mathbf{n}} \cdot k_l \nabla T_l, \quad (2.23)$$

where the advective contribution to the heat flux is negligible on both sides of the interface. Indeed, in the gas phase, conduction is the dominant contribution (due to the large value of thermal diffusivity  $\alpha_g$ ), while on the liquid side

$$\hat{\mathbf{n}} \cdot (\mathbf{u}_l - \mathbf{u}_i) = \frac{J}{\rho_l}. \quad (2.24)$$

Since the liquid density is much greater than that of the gas, the left-hand-side of (2.24) is very small compared with  $\hat{\mathbf{n}} \cdot (\mathbf{u}_g - \mathbf{u}_i)$  and can be ignored.

The remaining boundary conditions for  $\mathbf{u}$  and  $T$  at the liquid-vapour interface are standard: the temperature is continuous

$$T_l = T_i = T_v \quad (2.25)$$

as are the tangential velocity components

$$(1 - \hat{\mathbf{n}} \cdot \hat{\mathbf{n}})(\mathbf{u}_l - \mathbf{u}_g) = 0. \quad (2.26)$$

The stress balance

$$(\Sigma_l - \Sigma_g) \cdot \hat{\mathbf{n}} = \hat{\mathbf{n}} \kappa \sigma - \gamma \nabla_s T_i \quad (2.27)$$

incorporates both the viscous drag between the two phases and the thermocapillary effect. Here  $\Sigma = \mu [\nabla \mathbf{u} + (\nabla \mathbf{u})^T] - p$  is the stress tensor,  $\kappa \approx 0$  is the interfacial curvature,  $\nabla_s = (1 - \hat{\mathbf{n}} \cdot \hat{\mathbf{n}}) \nabla$  is the surface gradient, and  $\gamma = -\partial \sigma / \partial T$  is the temperature coefficient of surface tension.

### 3. The Base Flow

In liquid layers that are not too thin, under normal gravity, convection is driven by both buoyancy and thermocapillarity. Their strength can be quantified, respectively, in terms of the Marangoni number

$$Ma = \frac{\gamma d_l^2}{\mu_l \alpha_l} \tau \quad (3.1)$$

and the Rayleigh number

$$Ra = \frac{g \beta_l d_l^4 \tau}{\nu_l \alpha_l}, \quad (3.2)$$

where  $\nu_l = \mu_l / \rho_l$  is the kinematic viscosity of the liquid and  $\tau$  is the magnitude of the temperature gradient (measured at the interface). The dynamic Bond number

$$Bo_D = \frac{Ra}{Ma} = \frac{\rho_l g \beta_l d_l^2}{\gamma} \quad (3.3)$$

is independent of  $\tau$  and quantifies the relative strength of buoyancy and thermocapillarity. In defining nondimensional combinations, as well as various scales, we will use the values of parameters at the reference temperature  $T_0$ , which corresponds to global thermodynamic equilibrium. The superscript 0 is used throughout the paper to distinguish the equilibrium values from the nonequilibrium ones, where the choice is not obvious.

At sufficiently low  $Ma$ , a steady return flow is found in the liquid layer. An analytical solution for such a flow in laterally unbounded layers of nonvolatile liquids has been derived by Birikh (1966) using a one-sided model, which completely ignores the gas phase. This solution also accurately predicts the flow observed in laterally bounded layers away from the end walls when (i) phase change is negligible (e.g., when the gas is dominated by air,  $c_a^0 \approx 1$ ) and (ii) the temperature gradient  $\tau$  is sufficiently low (Qin *et al.* 2014). For volatile fluids, especially at reduced pressures, Birikh's solution becomes invalid due to the increasing role of phase change (Li & Yoda 2015; Qin & Grigoriev 2015). Instead, we should look for a solution to the two-sided model described in the previous section, which describes the flow in both layers. In order to reduce the number of parameters, the governing equations (2.1), (2.14), (2.15), and (2.16) are nondimensionalized by introducing the length scale  $d_l$ , time scale  $d_l^2 / \nu_l$ , velocity scale  $\nu_l / d_l$ , density scale  $\rho_l$ , pressure scale  $\rho_l (\nu_l / d_l)^2$ , and temperature scale  $\tau d_l = \mu_l \alpha_l Ma / (\gamma d_l)$ .

The dimensionless governing equations for the liquid layer become

$$\begin{aligned} \tilde{\nabla} \cdot \tilde{\mathbf{u}}_l &= 0, \\ \partial_{\tilde{t}} \tilde{\mathbf{u}}_l + \tilde{\mathbf{u}}_l \cdot \tilde{\nabla} \tilde{\mathbf{u}}_l &= -\tilde{\nabla} \tilde{p} + \tilde{\nabla}^2 \tilde{\mathbf{u}}_l + Gr \tilde{T}_l \hat{z}, \\ \partial_{\tilde{t}} \tilde{T}_l + \tilde{\mathbf{u}}_l \cdot \tilde{\nabla} \tilde{T}_l &= Pr^{-1} \tilde{\nabla}^2 \tilde{T}_l, \end{aligned} \quad (3.4)$$

where  $\tilde{\nabla} = d_l \nabla$ ,  $\tilde{\mathbf{u}}_l = \mathbf{u}_l d_l / \nu_l$ ,  $\tilde{T}_l = (T_l - T_0) / (\tau d_l)$ , and

$$Gr = \frac{Ra}{Pr} = \frac{g \beta_l d_l^4 \tau}{\nu_l^2} \quad (3.5)$$

is the Grashof number. We will use a coordinate system defined such that the liquid-vapour interface corresponds to the plane  $\tilde{z} = 0$  (so that the liquid layer corresponds to  $-1 < \tilde{z} < 0$ ) and the  $x$  axis points in the direction of the applied temperature gradient.

The dimensionless governing equations for the gas layer ( $0 < \tilde{z} < A$ ) are

$$\begin{aligned}\tilde{\nabla} \cdot \tilde{\mathbf{u}}_g &= 0, \\ \partial_{\tilde{t}} \tilde{\mathbf{u}}_g + \tilde{\mathbf{u}}_g \cdot \tilde{\nabla} \tilde{\mathbf{u}}_g &= -\frac{\rho_l}{\rho_g} \tilde{\nabla} \tilde{p} + K_\nu \tilde{\nabla}^2 \tilde{\mathbf{u}}_g + (\Xi_T \tilde{T}_g + \Xi_c \tilde{c}_v) \hat{z}, \\ \partial_{\tilde{t}} \tilde{T}_g + \tilde{\mathbf{u}}_g \cdot \tilde{\nabla} \tilde{T}_g &= K_\alpha \tilde{\nabla}^2 \tilde{T}_g, \\ \partial_{\tilde{t}} \tilde{c}_v + \tilde{\mathbf{u}}_g \cdot \tilde{\nabla} \tilde{c}_v &= K_D \tilde{\nabla}^2 \tilde{c}_v,\end{aligned}\tag{3.6}$$

where  $\tilde{\mathbf{u}}_g = \mathbf{u}_g d_l / \nu_l$ ,  $\tilde{T}_g = (T_g - T_0) / (\tau d_l)$ ,  $\tilde{c}_v = c_v - c_v^0$ ,  $c_v^0 = 1 - c_a^0$ ,  $A = d_g / d_l$ ,  $K_\nu = \nu_g / \nu_l$ ,  $K_\alpha = \alpha_g / \nu_l$ , and  $K_D = D / \nu_l$ . The nondimensional combinations

$$\begin{aligned}\Xi_T &= \frac{g \beta_g d_l^4 \tau}{\nu_l^2} = \frac{\beta_g}{\beta_l} Gr, \\ \Xi_c &= \frac{g d_l^3}{\nu_l^2} \frac{m_a - m_v}{c_a^0 m_a + c_v^0 m_v}\end{aligned}\tag{3.7}$$

describe the contributions to the buoyancy force in the gas layer due to perturbations in the temperature and composition of the gas, respectively. Note that  $\Xi_T$  depends on the imposed temperature gradient  $\tau$ , but not  $c_a^0$ , while  $\Xi_c$  depends on  $c_a^0$ , but not  $\tau$ .

Both the imposed temperature gradient  $\tau$  and the composition of the gas phase, parametrized by the equilibrium concentration of air  $c_a^0$ , play a key role in this problem. In experiment (Li & Yoda 2015),  $c_a^0$  was controlled indirectly by varying the net gas pressure

$$p_g^0 = \frac{p_v^0}{1 - c_a^0}.\tag{3.8}$$

In the following analysis, it will be more convenient to describe the composition directly in terms of  $c_a^0$ .

In order to satisfy the incompressibility condition, we will assume that the flow is strictly two-dimensional and introduce a stream function for each layer, such that

$$\begin{aligned}\tilde{\mathbf{u}}_l &= (\partial_{\tilde{z}} \tilde{\psi}_l, 0, -\partial_{\tilde{x}} \tilde{\psi}_l), \\ \tilde{\mathbf{u}}_g &= (\partial_{\tilde{z}} \tilde{\psi}_g, 0, -\partial_{\tilde{x}} \tilde{\psi}_g).\end{aligned}\tag{3.9}$$

Eliminating the pressure, the governing equations (3.4) for the liquid layer can be rewritten as

$$\begin{aligned}(\partial_{\tilde{t}} - \tilde{\nabla}^2 + \partial_{\tilde{z}} \tilde{\psi}_l \partial_{\tilde{x}} - \partial_{\tilde{x}} \tilde{\psi}_l \partial_{\tilde{z}}) \tilde{\nabla}^2 \tilde{\psi}_l + Gr \partial_{\tilde{x}} \tilde{T}_l &= 0, \\ \partial_{\tilde{t}} \tilde{T}_l + \partial_{\tilde{z}} \tilde{\psi}_l \partial_{\tilde{x}} \tilde{T}_l - \partial_{\tilde{x}} \tilde{\psi}_l \partial_{\tilde{z}} \tilde{T}_l - Pr^{-1} \tilde{\nabla}^2 \tilde{T}_l &= 0.\end{aligned}\tag{3.10}$$

For the gas layer we have

$$\begin{aligned}(\partial_{\tilde{t}} - K_\nu \tilde{\nabla}^2 + \partial_{\tilde{z}} \tilde{\psi}_g \partial_{\tilde{x}} - \partial_{\tilde{x}} \tilde{\psi}_g \partial_{\tilde{z}}) \tilde{\nabla}^2 \tilde{\psi}_g + \Xi_T \partial_{\tilde{x}} \tilde{T}_g + \Xi_c \partial_{\tilde{x}} \tilde{c}_v &= 0, \\ \partial_{\tilde{t}} \tilde{T}_g + \partial_{\tilde{z}} \tilde{\psi}_g \partial_{\tilde{x}} \tilde{T}_g - \partial_{\tilde{x}} \tilde{\psi}_g \partial_{\tilde{z}} \tilde{T}_g - K_\alpha \tilde{\nabla}^2 \tilde{T}_g &= 0, \\ \partial_{\tilde{t}} \tilde{c}_v + \partial_{\tilde{z}} \tilde{\psi}_g \partial_{\tilde{x}} \tilde{c}_v - \partial_{\tilde{x}} \tilde{\psi}_g \partial_{\tilde{z}} \tilde{c}_v - K_D \tilde{\nabla}^2 \tilde{c}_v &= 0.\end{aligned}\tag{3.11}$$

### 3.1. Boundary Conditions

At the bottom of the liquid layer ( $\tilde{z} = -1$ ) and the top of the gas layer ( $\tilde{z} = A$ ), no-slip and adiabatic boundary conditions apply

$$\begin{aligned}\tilde{\mathbf{u}} &= 0, \\ \partial_{\tilde{z}} \tilde{T} &= 0.\end{aligned}\tag{3.12}$$



At the interface ( $\tilde{z} = 0$ ), the temperature and velocity fields are continuous

$$\begin{aligned}\tilde{T}_l &= \tilde{T}_g = \tilde{T}_i, \\ \tilde{\mathbf{u}}_l &= \tilde{\mathbf{u}}_g = \tilde{\mathbf{u}}_i,\end{aligned}\tag{3.13}$$

where we can use the freedom of choosing the origin of our coordinate system to set  $\tilde{T}_i = \tilde{x}$ . Since  $\mu_l \gg \mu_g$  and typically  $d_g > d_l$ , the viscous stress in the gas layer can be ignored, yielding a simplified expression for the shear stress balance at the interface

$$\partial_{\tilde{z}} \tilde{u}_{l,x} = -Re \partial_{\tilde{x}} \tilde{T}_l,\tag{3.14}$$

where

$$Re = \frac{Ma}{Pr} = \frac{\gamma d_l^2}{\mu_l \nu_l} \tau,\tag{3.15}$$

is the Reynolds number.

The heat flux balance (2.23) at the interface reduces to

$$\partial_{\tilde{z}} \tilde{T}_l = \frac{k_g}{k_l} \partial_{\tilde{z}} \tilde{T}_g - \frac{V}{Ma} \tilde{J},\tag{3.16}$$

where  $k_g = c_v^0 k_v + c_a^0 k_a$ , and  $\tilde{J} = J d_l / (D m_v n_g)$  is the dimensionless mass flux. The dimensionless combination

$$V = \frac{\mathcal{L} \gamma d_l}{\alpha_l \mu_l k_l} \frac{D p_g^0}{\bar{R}_v T_0},\tag{3.17}$$

or more precisely the ratio  $V/Ma$ , describes the relative magnitude of the latent heat released (absorbed) at the interface due to condensation (evaporation) compared with the vertical heat flux in the liquid layer due to conduction. It should be noted that, although the product  $D p_g^0$ , and consequently  $V$ , is a function of  $T_0$ , it is independent of the gas pressure, and therefore  $c_a^0$ .

Non-dimensionalizing (2.21) and (2.22), we obtain

$$\partial_{\tilde{z}} \tilde{c}_v = -c_a^0 c_v^0 \tilde{J}\tag{3.18}$$

and

$$\hat{\mathbf{n}} \cdot (\tilde{\mathbf{u}}_g - \tilde{\mathbf{u}}_i) = c_v^0 K_D \tilde{J}.\tag{3.19}$$

The mass flux vanishes at the top of the gas layer

$$\partial_{\tilde{z}} \tilde{c}_v = 0.\tag{3.20}$$

The base uniform flow corresponds to a vanishing mass flux at the interface  $\tilde{J} = 0$ , which is also an assumption made in all one-sided models. We will also assume a nondeformable interface, so that  $\hat{\mathbf{n}} \cdot \tilde{\mathbf{u}}_i = 0$ . This leads to a number of simplifications. In particular, (3.18) and (3.19) require that  $\tilde{u}_{l,z} = \tilde{u}_{g,z} = 0$  and  $\partial_{\tilde{z}} \tilde{c}_v = 0$  at the interface. Furthermore, the heat flux at the interface should also vanish, so that (2.23) gives  $\partial_{\tilde{z}} \tilde{T}_l = \partial_{\tilde{z}} \tilde{T}_g = 0$ .

The boundary conditions for the stream functions can be easily obtained from those for the velocities. At the bottom of the liquid layer and the top of the gas layer

$$\begin{aligned}\tilde{\psi} &= 0, \\ \partial_{\tilde{x}} \tilde{\psi} &= \partial_{\tilde{z}} \tilde{\psi} = 0.\end{aligned}\tag{3.21}$$

Since for a uniform flow the net flux through any vertical plane vanishes, at the interface

$$\begin{aligned}\tilde{\psi}_l &= \tilde{\psi}_g = 0, \\ \partial_{\tilde{z}}\tilde{\psi}_l - \partial_{\tilde{z}}\tilde{\psi}_g &= 0, \\ \partial_{\tilde{z}}^2\tilde{\psi}_l + Re\partial_{\tilde{x}}\tilde{T}_l &= 0.\end{aligned}\tag{3.22}$$

### 3.2. Fluid Flow and Temperature in the Liquid Layer

For a horizontal flow, where both  $\tilde{\psi}_l$  and  $\tilde{\psi}_g$  are functions of  $\tilde{z}$  alone, we can look for solutions to (3.10) in the form

$$\tilde{T}_l = \tilde{x} + \tilde{\theta}_l(\tilde{z}),\tag{3.23}$$

where  $\tilde{\theta}_l(0) = 0$  such that  $T_i = T_0$  at  $x = 0$ . With this choice, the system (3.10) reduces to coupled ordinary differential equations (ODEs)

$$\begin{aligned}-\tilde{\psi}_l'''' + Gr &= 0, \\ Pr\tilde{\psi}_l' - \tilde{\theta}_l'' &= 0,\end{aligned}\tag{3.24}$$

where prime stands for the derivatives with respect to the  $\tilde{z}$  coordinate.

Solving the system (3.24) subject to the boundary conditions at the bottom and the free surface of the liquid layer, we find the steady state solutions for the stream function

$$\tilde{\psi}_l = Re \left[ -\frac{\tilde{z}(\tilde{z}+1)^2}{4} + Bo_D \frac{\tilde{z}(\tilde{z}+1)^2(2\tilde{z}-1)}{48} \right] \hat{x},\tag{3.25}$$

velocity

$$\tilde{\mathbf{u}}_l = Re \left[ -\frac{(\tilde{z}+1)(3\tilde{z}+1)}{4} + Bo_D \frac{(\tilde{z}+1)(8\tilde{z}^2 + \tilde{z} - 1)}{48} \right] \hat{x},\tag{3.26}$$

and temperature field

$$\tilde{T}_l = \tilde{x} + Ma \left[ -\frac{\tilde{z}^2(3\tilde{z}^2 + 8\tilde{z} + 6)}{48} + Bo_D \frac{\tilde{z}^2(8\tilde{z}^3 + 15\tilde{z}^2 - 10)}{960} \right]\tag{3.27}$$

describing the base flow. They agree with the analytical solutions originally obtained by Birikh (Birikh 1966) and later rederived by Kirdyashkin (Kirdyashkin 1984) and Villers and Platten (Villers & Platten 1987) using a one-sided model that ignores the effects of the gas phase.

The assumption that the interfacial temperature varies linearly has been widely used in previous studies without much justification, for deriving the solutions (3.26) and (3.27) for the return flow underlying the stability analyses (Parmentier *et al.* 1993; Mercier & Normand 1996; Priede & Gerbeth 1997) as well as in models of the adiabatic section of heat pipes (Ha & Peterson 1994; Suman & Kumar 2005; Markos *et al.* 2006), which assume unidirectional flow in the liquid phase. However, the validity of this assumption cannot be established by a one-sided model which ignores the transport in the gas phase. In fact, when  $c_a^0$  becomes sufficiently low, the interfacial temperature profile becomes nonlinear (Li & Yoda 2015; Qin & Grigoriev 2015). Proper justification of the linearity assumption requires showing that it is consistent with a steady-state solution of the transport equations in the gas phase, which satisfies all of the boundary conditions at the free surface. We do this next.

### 3.3. Fluid Flow, Temperature, and Composition in the Gas Layer

The solutions for the velocity, temperature, and composition of the gas phase can be found in the same way the solutions (3.26) and (3.27) were obtained for the liquid phase.

We will start by finding the solution for the vapour concentration at the interface before deriving the solution in the bulk. Since there is no phase change,  $T_s = T_i$ , according to (2.17), and  $\partial_x T_s = \tau$ . Using Clausius-Clapeyron relation (2.18) and neglecting the deviation of  $p_g$  from the equilibrium value (3.8) we therefore find

$$\partial_x c_v = \frac{\mathcal{L}\tau}{\bar{R}_v T_i^2} c_v, \quad (3.28)$$

where for  $\tau x \ll T_0$  we can replace  $T_i$  with the reference temperature  $T_0$ . In general, the solution to this equation yields an exponential concentration profile for  $c_v$  and hence a nonlinear interfacial temperature profile (Qin & Grigoriev 2015). However, when the deviation of  $c_v$  from  $c_v^0$  is small, the concentration profile at the interface becomes approximately linear

$$\tilde{c}_v \approx \Omega \tilde{x}, \quad (3.29)$$

where

$$\Omega = c_v^0 \frac{\mathcal{L} d_l \tau}{\bar{R}_v T_0^2} = c_v^0 \frac{H}{V} Ma, \quad (3.30)$$

and

$$H = \frac{\mathcal{L}^2 D p_g^0}{\bar{R}_v^2 T_0^3 k_l} \quad (3.31)$$

is another nondimensional parameter, the meaning of which will become clear later. Again, since the product  $D p_g^0$  is independent of  $c_a^0$ , so is  $H$ .

Given the boundary conditions for  $\tilde{T}_g$  and  $\tilde{c}_v$ , we can look for solutions to these two fields in the gas layer of the form

$$\begin{aligned} \tilde{T}_g &= \tilde{x} + \tilde{\theta}_g(\tilde{z}), \\ \tilde{c}_v &= \Omega[\tilde{x} + \tilde{\zeta}_v(\tilde{z})], \end{aligned} \quad (3.32)$$

where

$$\begin{aligned} \tilde{\theta}_g(0) &= 0, \\ \tilde{\zeta}_v(0) &= 0. \end{aligned} \quad (3.33)$$

For a uniform flow,  $\tilde{\psi}_g$  should only depends on  $\tilde{z}$ , so the system (3.11) reduces to

$$\begin{aligned} -\tilde{\psi}_g'''' + \Xi_T + \Xi_c \Omega &= 0, \\ \tilde{\psi}_g' - K_\alpha \tilde{\theta}_g'' &= 0, \\ \tilde{\psi}_g' - K_D \tilde{\zeta}_v'' &= 0. \end{aligned} \quad (3.34)$$

Solving these equations subject to the boundary conditions (3.20), (3.21), (3.22), and (3.33) at the interface and the top wall of the cell yields the steady state solutions for the stream function

$$\tilde{\psi}_g = -\mathcal{R} \left[ \frac{\tilde{z}(\tilde{z} - A)^2}{4A^2} + \mathcal{B} \frac{\tilde{z}(\tilde{z} - A)^2(2\tilde{z} + A)}{48A^3} \right] \hat{x}, \quad (3.35)$$

velocity

$$\tilde{\mathbf{u}}_g = -\mathcal{R} \left[ \frac{(\tilde{z} - A)(3\tilde{z} - A)}{4A^2} + \mathcal{B} \frac{(\tilde{z} - A)(8\tilde{z}^2 - A\tilde{z} - A^2)}{48A^3} \right] \hat{x}, \quad (3.36)$$

temperature

$$\tilde{T}_g = \tilde{x} - \frac{\mathcal{R}}{K_\alpha} \left[ \frac{\tilde{z}^2(3\tilde{z}^2 - 8A\tilde{z} + 6A^2)}{48A^2} + \mathcal{B} \frac{\tilde{z}^2(8\tilde{z}^3 - 15A\tilde{z}^2 + 10A^3)}{960A^3} \right], \quad (3.37)$$

and vapour concentration in the gas phase

$$\tilde{c}_v = \Omega\tilde{x} - \Omega \frac{\mathcal{R}}{K_D} \left[ \frac{\tilde{z}^2(3\tilde{z}^2 - 8A\tilde{z} + 6A^2)}{48A^2} + \mathcal{B} \frac{\tilde{z}^2(8\tilde{z}^3 - 15A\tilde{z}^2 + 10A^3)}{960A^3} \right]. \quad (3.38)$$

The parameters  $\mathcal{R}$  and  $\mathcal{B}$  are analogous to the Reynolds number and the dynamic Bond number, but incorporate the properties of both fluid layers:

$$\begin{aligned} \mathcal{R} &= Re \left( 1 + \frac{Bo_D}{12} \right) + \frac{A^3}{12K_\nu} (\Xi_T + \Xi_\varsigma), \\ \mathcal{B} &= -\frac{A^3}{\mathcal{R}K_\nu} (\Xi_T + \Xi_\varsigma). \end{aligned} \quad (3.39)$$

where we defined

$$\Xi_\varsigma = \Xi_c \Omega = -\frac{(1 - c_a^0)(\bar{R}_a - \bar{R}_v)}{\bar{R}_a - (\bar{R}_a - \bar{R}_v)c_a^0} \frac{\mathcal{L}\rho_l g d_l^2}{\bar{R}_v \gamma T^2} \frac{Ma}{Pr}. \quad (3.40)$$

Note that the form of the analytical solutions (3.26)-(3.27) and (3.36)-(3.38) is different from that of the solutions derived by Qin *et al.* (2014) because (i) the buoyancy force caused by the variation in the composition of the gas is explicitly taken into account in the present analysis, (ii) the mass transport in the gas phase is described using the molar fraction rather than the vapour mass density, and (iii) a different choice of the origin of the coordinate system is made.

#### 4. A Steady Patterned State

To date, only one study (Priede & Gerbeth 1997) of pattern formation in buoyancy-thermocapillary convection correctly predicted the formation of a stationary pattern of convection cells observed in experiment at  $Bo_D = O(1)$ . The study, however, was based on a one-sided model which completely ignored phase change and assumed adiabatic conditions at the free surface. While such description may be acceptable for nonvolatile liquids or at high concentrations of air, it fails to describe volatile liquids at lower concentrations of air. Below a generalized analysis is presented, which accounts for both heat and mass flux across the interface associated with phase change and which is applicable regardless of the amount of air present in the cell (e.g., the average concentration  $c_a^0$ ).

##### 4.1. Diffusion-Dominated Case

While the nondimensional equations (3.4) for the liquid layer can be used without modification, in order to obtain a simplified problem, which can generate useful physical insight, we will start by making several approximations in the treatment of heat and mass transport on the gas side. The relative contribution of advection and diffusion to the mass and heat transport in the gas layer are described by the Péclet numbers  $Pe_m$  and  $Pe_t$ , respectively. Since the relevant length scale here is the wavelength of the convective pattern, which is comparable to the depth of the liquid layer, and the velocity scale is determined by the interfacial velocity  $u_i = \nu_l \tilde{u}_l(0)/d_l$  (cf. Eq. (3.26)), we have

$$Pe_m = \frac{|u_i|d_l}{D} = \frac{12 + Bo_D}{48} \frac{Re}{K_D} \quad (4.1)$$

and

$$Pe_t = \frac{|u_i|d_l}{\alpha_g} = \frac{12 + Bo_D}{48} \frac{Re}{K_\alpha}. \quad (4.2)$$

In typical experiments (Villers & Platten 1992; Riley & Neitzel 1998; Li & Yoda 2015) both Péclet numbers are at most  $O(1)$ , so dropping the advective terms and the time derivatives in the transport equations (2.15) and (2.16) in the gas phase or, equivalently, replacing (3.11) with

$$\begin{aligned} \tilde{\psi}_g &= 0, \\ (\partial_x^2 + \partial_z^2)\tilde{T}_g &= 0, \\ (\partial_x^2 + \partial_z^2)\tilde{c}_v &= 0, \end{aligned} \quad (4.3)$$

should not have a dramatic effect on the results. It should be noted that neglecting the transient dynamics of the gas phase changes neither the critical Marangoni number nor the critical wavelength for stationary instabilities, so this simplification is fully justified, if one is only interested in the transition thresholds.

The base solution  $\tilde{\psi}_{l0}$ ,  $\tilde{T}_{l0}$  describing the uniform return flow in the liquid layer is given by (3.25)-(3.27). The base solution to (4.3) describing the gas layer in the diffusion-dominate case can be obtained by setting  $\mathcal{R} = 0$  in (3.37)-(3.38) which is equivalent to setting  $\tilde{\mathbf{u}}_g = 0$  ( $\tilde{\psi}_g = 0$ ) and gives:

$$\begin{aligned} \tilde{T}_{g0} &= \tilde{x}, \\ \tilde{c}_{v0} &= \Omega\tilde{x}. \end{aligned} \quad (4.4)$$

Although the base state satisfies the adiabatic boundary condition, perturbations in the temperature will give rise to heat and mass flux across the interface and, consequently, through the gas phase. Perturbed solutions can be written in the form of Fourier integrals

$$\begin{aligned} \tilde{\psi}_m &= \tilde{\psi}_{m0} + \int_{-\infty}^{\infty} \tilde{\psi}_{mq}(\tilde{z}) e^{iqx + \sigma_q t} dq, \\ \tilde{T}_m &= \tilde{T}_{m0} + \int_{-\infty}^{\infty} \tilde{\theta}_{mq}(\tilde{z}) e^{iqx + \sigma_q t} dq, \\ \tilde{c}_v &= \tilde{c}_{v0} + \Omega \int_{-\infty}^{\infty} \tilde{\zeta}_{vq}(\tilde{z}) e^{iqx + \sigma_q t} dq, \end{aligned} \quad (4.5)$$

where  $m = \{l, g\}$  denotes the phase,  $q$  is the wavenumber describing the variation in the horizontal direction, and  $\sigma_q$  is the temporal growth rate. The functions  $\tilde{\psi}_{mq}(\tilde{z})$ ,  $\tilde{\theta}_{mq}(\tilde{z})$ , and  $\tilde{\zeta}_{vq}(\tilde{z})$  define the vertical profile for the perturbations in, respectively, the stream function  $\tilde{\psi}$ , temperature  $\tilde{T}$ , and vapour concentration  $\tilde{c}_v$  with wavenumber  $q$ .

Rewriting (4.3) in terms of the perturbations, we obtain

$$\begin{aligned} \tilde{\psi}_{gq} &= 0, \\ \tilde{\theta}_{gq}'' &= q^2 \tilde{\theta}_{gq}, \\ \tilde{\zeta}_{vq}'' &= q^2 \tilde{\zeta}_{vq}. \end{aligned} \quad (4.6)$$

Temperature continuity at the interface requires

$$\tilde{\theta}_{gq}(0) = \tilde{\theta}_{lq}(0). \quad (4.7)$$

At the top of the gas layer we have

$$\begin{aligned}\tilde{\theta}'_{gq}(A) &= 0, \\ \tilde{\zeta}'_{vq}(A) &= 0.\end{aligned}\tag{4.8}$$

The solution of (4.6) satisfying these boundary conditions is

$$\tilde{\theta}_{gq}(\tilde{z}) = \frac{\cosh[q(\tilde{z} - A)]}{\cosh(qA)} \tilde{\theta}_{gq}(0).\tag{4.9}$$

The solution for the perturbation in the vapour concentration is analogous:

$$\tilde{\zeta}_{vq}(\tilde{z}) = \frac{\cosh[q(\tilde{z} - A)]}{\cosh(qA)} \tilde{\zeta}_{vq}(0),\tag{4.10}$$

where  $\tilde{\zeta}_{vq}(0)$  can be related to the perturbation in the interfacial temperature via the Clausius-Clapeyron relation (2.18)

$$\tilde{\zeta}_{vq}(0) = \tilde{\theta}_{gq}(0).\tag{4.11}$$

Fourier transforming (3.18) yields

$$\tilde{J}_q = -\frac{\Omega}{c_a^0} \tilde{\zeta}'_{vq}(0),\tag{4.12}$$

where  $\tilde{J}_q$  is the Fourier coefficient of  $\tilde{J}(\tilde{x})$ . Subtracting the base solutions from the heat balance (3.16), Fourier transforming the result, and using (4.12) gives the following relation

$$\tilde{\theta}'_{lq}(0) = \frac{k_g}{k_l} \tilde{\theta}'_{gq}(0) + \frac{\Omega}{c_a^0} \frac{V}{Ma} \tilde{\zeta}'_{vq}(0).\tag{4.13}$$

With the help of (4.9), (4.10), and (4.11) this can be rewritten in the form of Newton's cooling law

$$\tilde{\theta}'_{lq}(0) = -Bi_q \tilde{\theta}_{lq}(0),\tag{4.14}$$

where we introduced a wavenumber-dependent analogue of the Biot number

$$Bi_q = q \tanh(qA) \left[ \frac{k_g}{k_l} + \frac{1 - c_a^0}{c_a^0} H \right],\tag{4.15}$$

which will be referred to as the Biot coefficient below to highlight the fact that it is a function of  $q$  and  $c_a^0$ , not a constant. The prefactor  $\tanh(qA)$  describes the effect of finite thickness of the gas layer. For  $d_g \gg d_l$  ( $A \gg 1$ ), it approaches unity and (4.15) reduces to the expression derived by Chauvet *et al.* (Chauvet *et al.* 2012) in the context of stability of a volatile liquid layer in the presence of a *vertical* temperature gradient. The first term describes the effect of thermal conduction through the gas layer, while the second term describes the effect of latent heat released/absorbed at the interface as a result of condensation/evaporation.

By linearizing the governing equations (3.10) around the base state (3.25)-(3.27), we obtain the evolution equations for the perturbations  $\tilde{\psi}_{lq}$  and  $\tilde{\theta}_{lq}$  in the liquid layer

$$\begin{aligned}\tilde{\nabla}_q^2 \tilde{\nabla}_q^2 \tilde{\psi}_{lq} + iqC_1(\tilde{z}) Re \tilde{\psi}_{lq}'' - iqC_2(\tilde{z}) Re \tilde{\psi}_{lq} - iqGr \tilde{\theta}_{lq} &= \sigma_q \tilde{\nabla}_q^2 \tilde{\psi}_{lq}, \\ Pr^{-1} \tilde{\nabla}_q^2 \tilde{\theta}_{lq} + iqC_1(\tilde{z}) Re \tilde{\theta}_{lq} - iqC_3(\tilde{z}) Ma \tilde{\psi}_{lq} - \tilde{\psi}_{lq}' &= \sigma_q \tilde{\theta}_{lq},\end{aligned}\tag{4.16}$$

where we defined  $\tilde{\nabla}_q^2 = \partial_{\tilde{z}}^2 - q^2$  and

$$\begin{aligned} C_1(\tilde{z}) &= \frac{(\tilde{z}+1)(3\tilde{z}+1)}{4} - Bo_D \frac{(\tilde{z}+1)(8\tilde{z}^2 + \tilde{z} - 1)}{48}, \\ C_2(\tilde{z}) &= q^2 C_1(\tilde{z}) + \frac{3}{2} - Bo_D \frac{8\tilde{z} + 3}{8}, \\ C_3(\tilde{z}) &= \frac{\tilde{z}(\tilde{z}+1)^2}{4} - Bo_D \frac{\tilde{z}(\tilde{z}+1)^2(2\tilde{z}-1)}{48}. \end{aligned} \quad (4.17)$$

This is a system of ODEs which is fourth-order with respect to  $\tilde{\psi}_{lq}$  and second-order with respect to  $\tilde{\theta}_{lq}$  and hence needs a total of six boundary conditions. These boundary conditions are:

$$\begin{aligned} \tilde{\psi}_{lq}(-1) &= 0, \\ \tilde{\psi}'_{lq}(-1) &= 0, \\ \tilde{\theta}'_{lq}(-1) &= 0. \end{aligned} \quad (4.18)$$

at the bottom of the liquid layer and

$$\begin{aligned} \tilde{\psi}_{lq}(0) &= 0, \\ \tilde{\psi}''_{lq}(0) &= -iqRe\tilde{\theta}_{lq}(0) \end{aligned} \quad (4.19)$$

and

$$\tilde{\theta}'_{lq}(0) = -Bi_q \tilde{\theta}_{lq}(0) \quad (4.20)$$

at the free surface. In the subsequent discussion we will refer to the system (4.16) with the boundary conditions (4.18)–(4.20) as the enhanced one-sided model, since it incorporates the effect of the gas phase entirely through boundary conditions at the interface.

#### 4.2. Transient Dynamics in the Gas Layer

A more accurate description of the instability can be obtained by restoring the time dependence of the temperature and composition of the gas phase. This corresponds to replacing the Laplace equations (4.3) with

$$\begin{aligned} \partial_t \tilde{T}_g &= K_\alpha \tilde{\nabla}^2 \tilde{T}_g, \\ \partial_t \tilde{c}_v &= K_D \tilde{\nabla}^2 \tilde{c}_v. \end{aligned} \quad (4.21)$$

The corresponding equations for the perturbations are

$$\begin{aligned} \tilde{\psi}_{gq} &= 0, \\ \tilde{\theta}''_{gq} - q^2 \tilde{\theta}_{gq} &= \sigma_q K_\alpha^{-1} \tilde{\theta}_{gq}, \\ \tilde{\zeta}''_{vq} - q^2 \tilde{\zeta}_{vq} &= \sigma_q K_D^{-1} \tilde{\zeta}_{vq}. \end{aligned} \quad (4.22)$$

These equations should be solved subject to the boundary conditions (4.7), (4.8), (4.11), (4.18), (4.19) and

$$\tilde{\theta}'_{lq}(0) = -\frac{k_g}{k_l} \tilde{\theta}'_{gq}(0) - \frac{1 - c_a^0}{c_a^0} H \tilde{\zeta}'_{vq}(0), \quad (4.23)$$

which follows from the heat flux balance (3.16) and the mass flux balance (4.12) and replaces (4.14).

Note that, since both  $K_\alpha$  and  $K_D$  are typically large compared with unity, the terms on the right-hand-side of (4.22) are small. Dropping them would lead to the formulation derived in Section 4.1.

#### 4.3. The Effect of Advection in the Gas Layer

The effect of advection can also be incorporated for the range of  $c_a^0$  where the base solution (3.35)-(3.38) is valid. By setting  $\tilde{\psi}_{gq} \neq 0$  we ensure that all of the transport mechanisms in the gas phase are accounted for and both layers are treated using an equally comprehensive model. The linearized evolution equations for the perturbations  $\tilde{\psi}_{gq}$ ,  $\tilde{\zeta}_{vq}$ , and  $\tilde{\theta}_{gq}$  in the gas phase are

$$\begin{aligned} \tilde{\nabla}_q^2 \tilde{\nabla}_q^2 \tilde{\psi}_{gq} + iq\tilde{C}_1(\tilde{z})\mathcal{R}\tilde{\psi}_{gq}'' - iq\tilde{C}_2(\tilde{z})\mathcal{R}\tilde{\psi}_{gq} - iq\Xi_T\tilde{\theta}_{gq} - iq\Xi_\zeta\tilde{\zeta}_{vq} &= \sigma_q \tilde{\nabla}_q^2 \tilde{\psi}_{gq}, \\ K_\alpha \tilde{\nabla}_q^2 \tilde{\theta}_{gq} + iq\tilde{C}_1(\tilde{z})\mathcal{R}\tilde{\theta}_{gq} - iq\tilde{C}_3(\tilde{z})\mathcal{R}K_\alpha^{-1}\tilde{\psi}_{gq} - \tilde{\psi}_{gq}' &= \sigma_q \tilde{\theta}_{gq}, \\ K_D \tilde{\nabla}_q^2 \tilde{\zeta}_{vq} + iq\tilde{C}_1(\tilde{z})\mathcal{R}\tilde{\zeta}_{vq} - iq\tilde{C}_3(\tilde{z})\mathcal{R}K_D^{-1}\tilde{\psi}_{gq} - \tilde{\psi}_{gq}' &= \sigma_q \tilde{\zeta}_{vq}. \end{aligned} \quad (4.24)$$

where

$$\begin{aligned} \tilde{C}_1(\tilde{z}) &= \frac{(\tilde{z} - A)(3\tilde{z} - A)}{4A^2} + \mathcal{B} \frac{(\tilde{z} - A)(8\tilde{z}^2 - A\tilde{z} - A^2)}{48A^3}, \\ \tilde{C}_2(\tilde{z}) &= q^2 \tilde{C}_1(\tilde{z}) + \frac{3}{2A^2} + \mathcal{B} \frac{8\tilde{z} - 3A}{8A^3}, \\ \tilde{C}_3(\tilde{z}) &= \frac{\tilde{z}(\tilde{z} - A)^2}{4A^2} + \mathcal{B} \frac{\tilde{z}(\tilde{z} - A)^2(2\tilde{z} + A)}{48A^3}. \end{aligned} \quad (4.25)$$

The boundary conditions are given by (4.7), (4.8), (4.11), (4.18), (4.19), (4.23). In addition, the boundary conditions for  $\tilde{\psi}_{gq}(\tilde{z})$  follow from (3.21) and (3.22):

$$\begin{aligned} \tilde{\psi}_{gq}(A) &= 0, \\ \tilde{\psi}_{gq}'(A) &= 0 \end{aligned} \quad (4.26)$$

at the top of the gas layer and

$$\begin{aligned} \tilde{\psi}_{gq}(0) &= 0, \\ \tilde{\psi}_{gq}'(0) &= \tilde{\psi}_{lq}'(0) \end{aligned} \quad (4.27)$$

at the free surface. In the subsequent discussion we will refer to the system (4.16) and (4.24) with the boundary conditions described in the previous paragraph as the two-sided model, since it treats both the liquid and gas phase with the same level of detail.

#### 4.4. Stationary Instability

The boundary value problem (whether it is (4.16) by itself or combined with (4.22) or (4.24)) has a spectrum of solutions  $(\sigma_q^n, \{\psi_{lq}^n, \theta_{lq}^n, \dots\})$  for a given complex wavenumber  $q = k + is$  and Marangoni number  $Ma$ . The threshold of the instability with respect to a stationary pattern corresponds to the eigenvalue with the largest real part (let's call it  $\sigma_q^0 = \alpha_q + i\omega_q$ ) vanishing. This defines two conditions,

$$\begin{aligned} \alpha_q(Ma_c, q_c) &= 0, \\ \omega_q(Ma_c, q_c) &= 0, \end{aligned} \quad (4.28)$$

for two unknowns, the critical wavenumber  $k_c$  and the critical Marangoni number  $Ma_c$ , which both depend on the spatial attenuation rate  $s$ .

Note that, for  $\sigma_q = 0$ , equations (4.22) reduce to (4.6) even if  $K_\alpha$  and  $K_D$  are not large. Hence the two formulations always give identical predictions for the transition thresholds (even though they predict different growth rates for modes with wavenumbers  $q$  different from the critical one). Therefore, in what follows we will only focus on the limits when either both  $Pe_m$  and  $Pe_t$  are vanishingly small and stability is described by (4.16) alone, or when they are both  $O(1)$ , so (4.16) and (4.24) have to be solved simultaneously.



The boundary value problems, which determine the stability of the flow, were solved using the function **bvp5c** in Matlab 2013a (cf. Appendix A for details) and the equations (4.28) were solved using a Newton solver.

## 5. Results

The boundary conditions in this problem are of the “enhancing” type (Cross & Greenside 2009): for  $Bo_D = O(1)$  the pattern (a single steady convection roll) emerges near the hot end wall at an arbitrarily small value of  $Ma$ . Riley & Neitzel (1998) refer to this state as a steady unicellular flow (SUF). In the core region of the flow, away from the end walls, convection is only observed for  $Ma$  above some threshold value (Villers & Platten 1992; De Saedeleer *et al.* 1996; Garcimartín *et al.* 1997; Riley & Neitzel 1998; Qin *et al.* 2014; Li & Yoda 2015; Qin & Grigoriev 2015). Since the perturbation strength is always  $O(1)$  at the hot end wall, defining the threshold values  $Ma_c$  and  $k_c$  for the transition, especially in systems of finite length  $L_x$ , requires some care.

In laterally infinite systems the transition threshold  $Ma_0$  is well-defined and corresponds to a purely real value of the critical wavenumber  $q_c = k_c$  and, correspondingly, a spatially uniform pattern ( $s = 0$ ). This will be referred to as the steady multicellular state (SMC) below. For  $Ma < Ma_0$  the convection pattern may not extend across the entire length of the system. In this case  $s = \text{Im}(q_c)$  defines the spatial attenuation of the perturbation (or the number of convection rolls that can be detected in the liquid layer), while  $k_c = \text{Re}(q_c)$  determines the wavelength of the pattern  $\lambda/d_l = 2\pi/k_c$  (or the distance between convection rolls). When  $e^{-|s|\Gamma_x} \ll 1$ , where  $\Gamma_x = L_x/d_l$  is the aspect ratio of the liquid layer, the pattern extends over a region of length  $O(2d_l/|s|) < L_x$ . We will refer to this as a partial multicellular regime (PMC) following Qin & Grigoriev (2015) and Li & Yoda (2015). In this analysis, we set  $s_{\text{PMC}} = -1$  to define the transition from SUF to PMC (which roughly corresponds to one extra roll near the hot end wall that can be detected). As  $Ma$  is increased, the convection pattern extends from the hot end wall further and further towards the cold end wall, until it covers the entire liquid layer. In practice this roughly corresponds to  $e^{-|s|\Gamma_x} \approx 0.1$  or  $|s_{\text{SMC}}| \approx 2/\Gamma_x$ . This is the definition that has to be used for  $Pr \lesssim 1$  (i.e., for metallic liquids featuring sensitive dependence of  $Ma$  on  $s$ , as shown below). For typical (non-metallic) liquids with  $Pr \gtrsim 2$ , we can set  $|s_{\text{SMC}}| \approx 0$ , as in the case of laterally unbounded layers, as long as  $\Gamma_x \gtrsim 10$ . This is the case in both the experimental (Riley & Neitzel 1998; Li & Yoda 2015) and numerical studies (Qin *et al.* 2014; Qin & Grigoriev 2015) used for comparison below.

Previous theoretical studies of stability focused mainly on the dependence of the critical Marangoni number  $Ma$  on the dynamic Bond number  $Bo_D$  and Prandtl number  $Pr$  characterizing the liquid layer. We have also investigated how both the critical  $Ma$  and the critical wavelength  $\lambda$  depend on the average concentration  $c_a^0$  of air. Where possible, the predictions of linear stability analysis have been compared with the available experimental and numerical data.

### 5.1. Convection at atmospheric conditions

Riley & Neitzel (1998) determined the dependence of both the critical  $Ma$  and the critical wavelength  $\lambda$  corresponding to the onset of steady multicells (SMC) on the dynamic Bond number  $Bo_D$  for the 1 cSt silicone oil with  $Pr = 13.9$ . In their study, the transition threshold for SMC is identified as the instance when multiple convection rolls appear near the hot end wall, but they do not extend all the way to the cold end wall, which is not a very precise definition. However, the experimental data should lie between the analytical prediction for the onset of PMC and SMC. Since Riley & Neitzel (1998) have

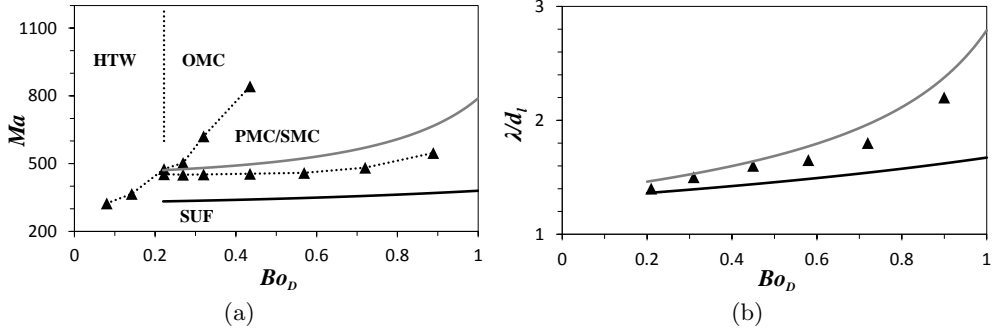


FIGURE 1.  $Bo_D$ -dependence of the critical Marangoni number (a) and the critical wavelength (b) for the 1.0 cSt silicone oil at atmospheric conditions ( $c_a^0 = 0.995$ ). Experimental results obtained by Riley & Neitzel (1998) are shown as black filled symbols and dotted lines, analytical predictions of the two-sided model for transition to the PMC (SMC) states are shown as black (gray) lines.

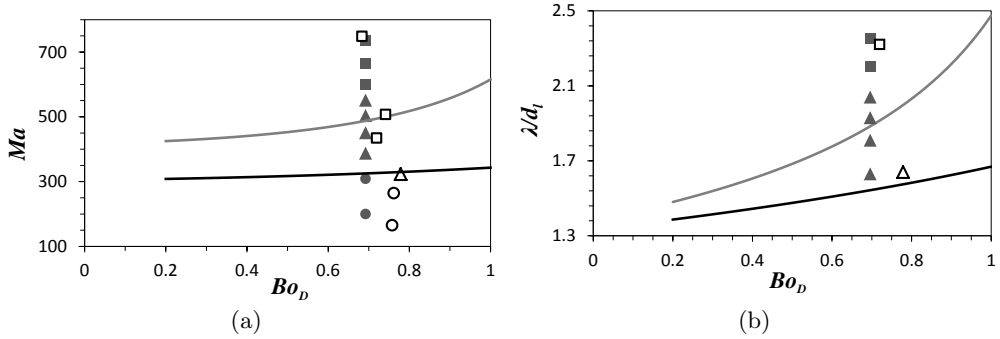


FIGURE 2.  $Bo_D$ -dependence of the critical Marangoni number (a) and the critical wavelength (b) for the 0.65 cSt silicone oil at atmospheric conditions ( $c_a^0 = 0.96$ ). The black (gray) lines corresponds to onset of the PMC (SMC) state. Open symbols correspond to experimental results of Li *et al.* (2014) and filled symbols – to numerical results of Qin *et al.* (2014). The four distinct flow regimes are: SUF ( $\circ$ ), PMC ( $\triangle$ ), SMC ( $\square$ ), and OMC ( $\diamond$ ).

not reported the values of all material parameters of the liquid, we took the missing ones from Kavehpour *et al.* (2002). No data has been found for the material properties of the vapour; these were assumed to be the same as those of the 0.65 cSt silicone oil (Yaws 2003, 2009). Any potential uncertainty in the values of these material parameters, however, will have a negligible effect on the results. The 1.0 cSt silicone oil is not particularly volatile (vapour pressure is  $p_v = 0.5$  kPa at  $T = 298$  K), therefore the properties of the gas phase are essentially those of air ( $c_a^0 = 0.995$  at atmospheric conditions).

As shown in Fig. 1, both the critical  $Ma$  and the critical wavelength  $\lambda$  observed in the experiments are indeed bracketed by the theoretical values corresponding to the onset of PMC and SMC, and lie closer to the SMC boundary in the entire range of  $Bo_D$  investigated in the experiment, where stationary convective patterns are observed. Riley and Neitzel's supporting figures show the presence of multiple convection rolls at the critical  $Ma$ , so their threshold values should be closer to the SMC threshold than the PMC threshold predicted by our linear stability analysis. The predictions of the enhanced one-sided model are essentially identical and therefore are not shown separately.

Next we compare the analytical predictions with the results of numerical and exper-

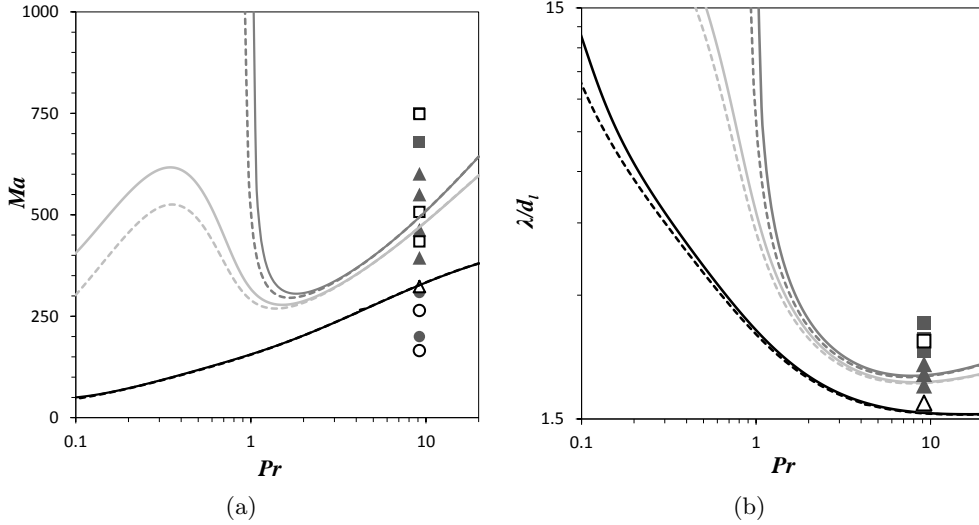


FIGURE 3.  $Pr$ -dependence of the critical Marangoni number (a) and the critical wavelength (b) at varying  $s$  for  $Bo_D = 0.72$  at atmospheric conditions ( $c_a^0 = 0.96$ ). The solid lines correspond to the prediction of linear stability analysis based on the two-sided model, and the dashed lines – the enhanced one-sided model. Black, dark gray and light gray lines correspond to  $s = -1$  (onset of the PMC state),  $s = 0$  (onset of the SMC state), and  $s = -0.1$ , respectively. The meaning of the symbols is the same as that in Fig. 2.

imental studies (Qin *et al.* 2014; Qin & Grigoriev 2015; Li *et al.* 2014), which used a more volatile liquid (0.65 cSt silicone oil) and characterized both the SMC→PMC and PMC→SMC transition. The predicted dependence on the dynamic Bond number at atmospheric conditions ( $c_a^0 = 0.96$ ) is shown in Fig. 2. Again, the predictions of the one- and two-sided model are essentially indistinguishable and are in reasonable agreement with both experimental and numerical data.

Just as in the case of the 1 cSt silicone oil, the critical values of  $Ma$  and  $\lambda$  increase monotonically with  $Bo_D$  over the range where a stationary pattern is found. This increase in  $Ma$  can be easily understood by noting that buoyancy has a stabilizing effect on the flow. The base flow solution (3.27) shows that the temperature increases, and hence the density of the liquid decreases, with height. An increase in  $Bo_D$  therefore corresponds to an increasingly strong effect of the stable density stratification.

The dependence of the threshold values of  $Ma$  and  $\lambda$  on the Prandtl number of the liquid has previously been investigated only in the context of linear stability analysis. In particular, Priede & Gerbeth (1997), who only considered uniform disturbances ( $s = 0$ ) and ignored heat and mass flux across the interface, found that the critical  $Ma$  for a stationary instability diverges at  $Pr_0 = O(1)$ . Our results shown in Fig. 3 demonstrate that this result also holds once transport in the gas phase has been taken into account. For  $Bo_D = 0.72$ , the critical  $Ma$  for SMC reaches a minimum at  $Pr \approx 1.6$ , and diverges at  $Pr_0 \approx 1$ . Over the entire range of  $Pr$  corresponding to non-metallic liquids,  $Ma_c$  is a monotonically increasing function. The dependence of the critical wavelength on the Prandtl number is also nonmonotonic;  $\lambda$  has a minimum at  $Pr \approx 8$  and diverges at  $Pr_0$ .

These results, however, do not imply that no stationary pattern emerges at  $Pr < Pr_0$ . Indeed, the critical  $Ma$  for PMC ( $s = -1$ ) decreases monotonically as  $Pr$  decreases, with  $Ma_c \rightarrow 0$  as  $Pr \rightarrow 0$ . As  $Ma$  increases, the spatial extent of the pattern increases as well. For a moderate value of  $Ma \approx 600$ , the pattern is predicted to extend across

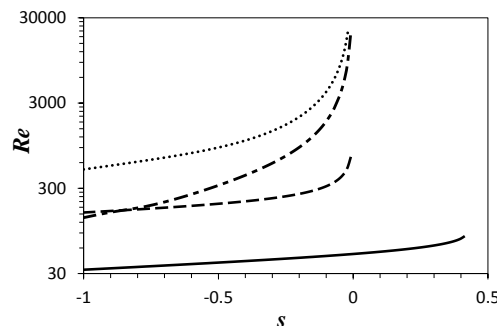


FIGURE 4. The critical Reynolds number for a fixed  $Bo_D = 0.72$  and atmospheric conditions ( $c_a^0 = 0.96$ ) and varying  $s$  and  $Pr$ : solid line ( $Pr = 10$ ), dashed line ( $Pr = 1$ ), dotted line ( $Pr = 0.1$ ) and dash-dotted line ( $Pr = 0.01$ ).

the entire liquid layer for *any*  $Pr$ , even for aspect ratios as large as  $\Gamma_x = 20$  (very few studies have ever considered larger aspect ratios), which corresponds to  $s = -0.1$ . The maximum of  $Ma_c$  is found to occur at  $Pr_0 = 0.33$  for  $s = -0.1$  and is expected to increase with decreasing  $|s|$ . The maximum value of  $Ma_c$  depends on the model: the enhanced one-sided model predicts  $Ma = 525$ , while the two-sided model predicts  $Ma = 617$  at  $Pr_0$ . The threshold of SMC at low  $Pr$  is the only example where the predictions of the enhanced one-sided model deviates significantly from that of the two-sided model. We will discuss the reasons behind this deviation in the next section.

As noted in the introduction, the analysis of Mercier & Normand (2002) predicted that, convection rolls should develop near the hot end for  $Pr > 4$ , near the cold end for  $Pr < 0.01$  or at both end walls for  $0.01 < Pr < 4$ . Our results unequivocally contradict that prediction. The Marangoni number becomes meaningless at low  $Pr$  since it describes the minute variation in the temperature field in the vertical direction that cannot be measured in experiment. Instead, we use the Reynolds number  $Re = Ma/Pr$  which characterizes the variation in the flow velocity, which is directly and easily measurable. As our results (cf. Fig. 4) illustrate, the critical  $Re$  is a monotonically increasing function of the spatial growth rate  $s$ , regardless of the value of  $Pr$ , indicating that the pattern *always* emerges first near the hot end wall. In fact, the critical  $Re$  diverges at  $|s| \approx 0$  for all  $Pr < Pr_0 \approx 1$ , indicating that, for a sufficiently large aspect ratio  $\Gamma_x$ , a disturbance localized near the cold end wall is stable and will dissipate at any finite  $Re$ .

Even though phase change is greatly suppressed at atmospheric conditions, this does not mean that the effect of mass and heat transport through the gas phase is negligible. In order to quantify how large this effect is, we compare the predictions of the two-sided model and those of the enhanced one-sided model with the adiabatic boundary condition  $Bi = 0$ . The latter should exactly reproduce the results of Priede & Gerbeth (1997). Fig. 5 shows the critical  $Ma$  for both the 1 cSt and 0.65 cSt silicone oil. Not surprisingly, we find that transport of heat and mass through the gas phase delays both the transition from SUF to PMC and the transition from PMC to SMC. Even though the 0.65 cSt silicone oil is substantially more volatile than the 1 cSt silicone oil, the relative difference between the predictions of the two models is roughly the same at a fixed  $Bo_D$  and increases with  $Bo_D$ . For example, at  $Bo_D = 0.72$ , the critical  $Ma$  increases by 2-3% for onset of the PMC state and by 3-5% for onset of the SMC state for both silicone oils considered here. The difference increases rather dramatically, however, once the pressure is reduced below the atmospheric value, as we show below.

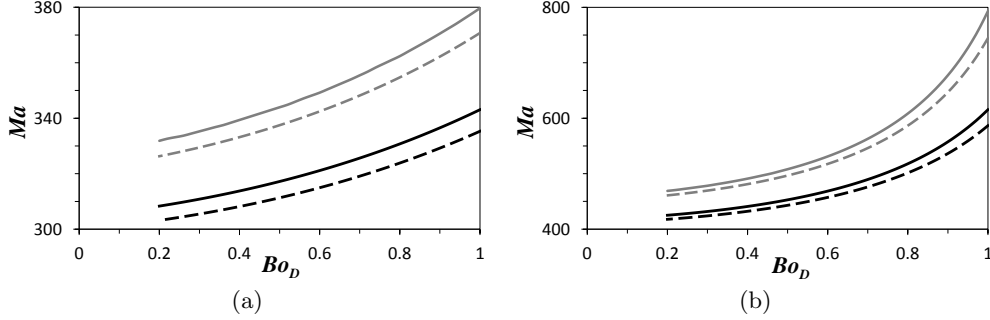


FIGURE 5. The critical Marangoni number for the PMC (a) and SMC (b) state at atmospheric conditions. Black lines describe the 0.65 cSt silicone oil ( $Pr = 9.19$ ,  $c_a^0 = 0.96$ ) and gray lines – the 1 cSt silicone oil ( $Pr = 13.9$ ,  $c_a^0 = 0.995$ ). Solid lines represent results of the two-sided model, dashed lines – the enhanced one-sided model with the adiabatic interface.

### 5.2. Convection at reduced pressures

In this section we will discuss the dependence of the critical  $Ma$  on the average concentration  $c_a^0$  of air. We will focus exclusively on the 0.65 cSt silicone oil and  $Bo_D = 0.72$ , since these are the only values for which relevant numerical or experimental data exist. The predictions of the one- and two-sided models are compared with that data in Fig. 6. The results of the two models are essentially identical, except for low  $c_a^0$ , where the validity of the assumptions underlying both models is questionable, as discussed below. The predicted  $Ma_c$  increases rather significantly as  $c_a^0$  is decreased from the atmospheric values down to the regime when the gas is dominated by the vapour, rather than air.

The predictions of the linear linear stability analysis are consistent with the experimental data, although at atmospheric conditions the predicted thresholds for the onset of PMC and SMC states are higher by about 20% compared with those found in experiment (cf. Fig. 6(a)). Numerical simulations have only been performed in the limits when either air or vapor dominate. When the gas phase is dominated by air ( $c_a^0 \geq 0.85$ ), the predictions of linear stability analysis for the onset of PMC are within the transition range found in the numerical simulations, while the predicted threshold of SMC is lower by about 20% compared with that found in the numerics. When the vapour is dominant ( $c_a^0 \leq 0.16$ ), the numerical simulations only find the SUF flow over the limited range of  $\Delta T$  considered, so no prediction of  $Ma_c$  can be made. However, the available numerical results support the theoretical predictions.

The dependence of the critical wavelength on  $c_a^0$  shows a similar trend: the predicted  $\lambda$  increases as  $c_a^0$  decreases (cf. Fig. 6(b)) and, at low  $c_a^0$ , becomes comparable to the length  $L$  of the cavity. These predictions are also in reasonable agreement with the available numerical and experimental results (Li & Yoda 2015). When the gas phase is dominated by air ( $c_a^0 \geq 0.85$ ), linear stability analysis underpredicts the critical wavelength for both the PMC and SMC state by about 6% compared with the values found in the numerics. Only experimental data is available for lower  $c_a^0$  and it is consistent with theoretical predictions over the entire range of air concentrations: the wavelength of the pattern is found to lie between the PMC and SMC curves, as it should.

The linear stability analysis assumes a flat interface and will break down for  $\lambda \gg d_l$ , when the thickness of the liquid layer is expected to vary noticeably, even if the layer were unbounded. Therefore, the theoretical predictions at low  $c_a^0$  (and also at low  $Pr$ ) are not expected to be particularly accurate. Furthermore, for sufficiently low  $c_a^0$ , and/or long cavities, the interfacial temperature profile in the SUF state deviates significantly

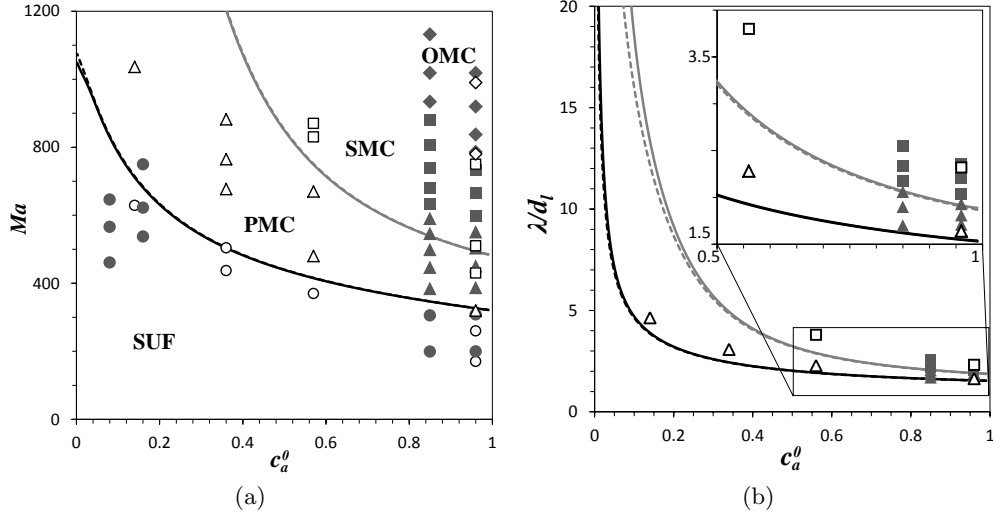


FIGURE 6.  $c_a^0$ -dependence of the critical Marangoni number (a) and wavelength (b) for the 0.65 cSt silicone oil with  $Bo_D = 0.72$ . The meaning of the symbols is the same as that in Fig. 2.

from linear, resulting in the breakdown of the analytical solution for the base flow (Qin & Grigoriev 2015).

## 6. Discussion

As our results illustrate, the predictions of the linear stability analysis based on the two-sided model are in general agreement with the reported numerical and experimental data. In particular, this analysis correctly predicts that the transitions between different flow regimes (SUF, PMC, SMC) are delayed (i.e., shifted towards higher  $Ma$ ) when the concentration of air decreases, although quantitative agreement is not expected at low  $c_a^0$  when the assumption of uniform temperature gradient breaks down and the analytical solution describing the base flow becomes invalid. The general agreement found at higher  $c_a^0$  confirms the validity of the assumptions made in the linear stability analysis, giving us confidence that it captures all the essential physical processes governing the flow stability for volatile liquids driven by a horizontal temperature gradient.

The discrepancy between the linear stability analysis and the numerical results is likely a result of insufficient resolution of the simulations. While adaptive mesh refinement used by Qin *et al.* (2014) and Qin & Grigoriev (2015) generated a fairly fine mesh (1/16 mm) in the liquid phase and near the end walls, a much coarser mesh was used in the core region of the gas phase. The discrepancy with the experiment can be due to a number of different reasons. One is the effect of transverse confinement: the liquid is wetting and rises at the side walls, increasing the thickness of the liquid layer there by up to 60%. The experimental study by Li & Yoda (2015) used the (smaller) thickness  $d_l$  of the liquid layer at the mid-plane of the cavity to compute  $Ma$ . Furthermore, the experimental study indirectly deduced the interfacial temperature gradient rather than measure it directly, which introduces additional uncertainty into the reported values of  $Ma$ .

In this problem, buoyancy plays a stabilizing role, hence the instability leading to the formation of convection rolls is driven primarily by thermocapillary stresses, which depend on the interfacial temperature gradient. The fluctuations in the interfacial tem-

perature are significantly affected by the heat and mass transport through the gas phase, which can be described using the Biot coefficient  $Bi_q$ , which is a function of both the wavenumber  $q$  and the concentration of air  $c_a^0$ . The first term in the square brackets in (4.15) describes the effect of conductive heat transport through the gas layer, and reflects the dependence of thermal conductivity of the gas phase on the gas composition, while the second term describes the effect of the latent heat released or absorbed at the interface as a result of phase change, and reflects the variation in the diffusive transport of vapour through the gas phase, which also depends on the gas composition. Both heat and mass transport through the gas phase suppress the fluctuations in the interfacial temperature.

To see the relative impact of the heat and mass transport on stability, it is instructive to compare the trends and characteristic magnitudes of the two terms. For the 0.65 cSt silicone oil used in this study, as  $c_a^0$  decreases, the first term decreases slightly (thermal conductivity of the vapour is somewhat smaller than that of the air), but the second term increases significantly, reflecting the enhancement of phase change. At atmospheric conditions, the heat flux in the gas phase has a slightly larger effect (the magnitudes of the first and second terms in the square brackets are 0.23 and 0.16, respectively). The effect of phase change becomes dominant for  $c_a^0 < 0.94$  and increases as  $c_a^0$  decreases (e.g., for  $c_a^0 = 0.1$ , the magnitudes of the first and second terms in the square brackets are 34.1 and 0.11, respectively). In fact, the second term diverges as  $c_a^0 \rightarrow 0$  which, according to (4.14), implies that the temperature fluctuations at the interface vanish and the critical  $Ma$  becomes infinite.

The increase in the critical  $Ma$  with decreasing  $c_a^0$  is due primarily to the enhancement of phase change which increases the amount of latent heat released/absorbed by the warmer/cooler regions of the interface, thereby suppressing the fluctuations in the interfacial temperature gradient. The composition of the gas phase has a more significant effect on flow stability than the base flow itself. As discussed by Qin & Grigoriev (2015), the concentration of air has a relatively weak effect on the base flow, since the average interfacial temperature gradient, which determines the thermocapillary stresses and hence the speed of the base flow, is insensitive to  $c_a^0$  above 10% or so.

Since the heat and mass transport through the gas phase significantly affect the flow stability, one-sided models, which neglect these effects, are incapable of predicting the transition thresholds for volatile fluids accurately. As discussed previously, even at atmospheric conditions, when phase change is strongly suppressed, one-sided models with the adiabatic boundary condition underestimate the critical  $Ma$  corresponding to the transition thresholds. At reduced pressures, heat and mass transport through the gas phase are significantly enhanced, and one-sided models produce very inaccurate results, since they completely fail to describe these effects.

To illustrate the deficiency of one-sided models, it is useful to focus on the dimensionless combinations that have been introduced over the years to describe the deviation from thermodynamic equilibrium, which gives rise to convection in the presence of evaporation. In particular, in their analysis of pure Marangoni (thermocapillary) instability in volatile fluids subjected to a *vertical* temperature gradient, Burelbach *et al.* (1988) introduced two nondimensional parameters, the evaporation number

$$E = \frac{k_l \Delta T}{\rho_l \nu_l \mathcal{L}}, \quad (6.1)$$

which defines the ratio of the evaporative time scale (how long it would take for a liquid layer to evaporate completely) to the viscous time scale, and the “non-equilibrium

parameter”

$$K = \frac{2\chi}{2 - \chi} \sqrt{\frac{\bar{R}_v T_0}{2\pi}} \frac{\rho_v \mathcal{L}^2 d_l}{k_l \bar{R}_v T_0^2}, \quad (6.2)$$

which defines the ratio of the latent heat flux at the interface to the conductive heat flux in the liquid. The stability analysis of this problem was performed correctly only recently by Chauvet *et al.* (2012) who found that a version of the Biot coefficient (4.15) appears there as well. However, neither  $E$  nor  $K$  appears in the stability analysis, regardless of the direction of the temperature gradient, because both parameters fail to account for the transport (of either heat or mass) in the gas phase. Instead, the Biot coefficient involves a nondimensional combination  $H$  defined by (3.31) which describes the effect of the latent heat associated with phase change and explicitly takes into account the mass transport in the gas phase.

The study by Normand *et al.* (1977) was probably the first to note that the Biot “number” should depend on the wavenumber for convective flows. In their analysis of buoyancy-thermocapillary convection driven by a horizontal temperature gradient, Mercier & Normand (1996) repeated that statement, but proposed to use the definition

$$Bi = \frac{k_g d_l}{k_l d_g} \quad (6.3)$$

based on conduction in the two layers instead. Although wavenumber-independent, this definition is similar in form to the correct one in the limit of an infinitely thick gas layer. Indeed, if we ignore phase change, for  $d_g \gg d_l$ , the expression (4.15) would reduce to

$$Bi_q = q \frac{k_g}{k_l} = 2\pi \frac{k_g d_l}{k_l \lambda}. \quad (6.4)$$

Here the wavelength of the pattern effectively plays the role of the gas layer thickness, the result that follows immediately from the second equation in (4.3) which controls the heat transport in the gas phase.

The wavenumber dependence of the Biot coefficient (4.15) implies that, once transformed to the real space, Newton’s cooling law

$$d_l \hat{\mathbf{n}} \cdot \nabla T_l = -Bi(T_i - T_0) \quad (6.5)$$

becomes invalid and has to be replaced by a spatially nonlocal relation between the interfacial temperature and the normal temperature gradient (or heat flux) in the liquid phase. Given that the Biot number (6.3) describes one-dimensional conduction, it is not surprising that (6.5) fails when spatial variation of the solution in the extended direction(s) is taken into account.

Finally, by comparing the results of linear stability analysis based on models of the gas layer that incorporate a varying level of detail, we found that advection (of both heat and mass) plays a relatively minor role and can be ignored except for  $Pr \lesssim 1$  (e.g., mostly for liquid metals). In this limit, the two-sided model, which accounts for advection in the gas layer predicts a somewhat higher critical  $Ma$  for the transition from PMC to SMC. This increase can be readily understood by considering the associated changes in the Péclet numbers (4.1) and (4.2), which are both proportional to  $Re = Ma/Pr$ . The enhanced advective transport in the gas phase at low  $Pr$  tends to suppress the variation in the temperature at the interface, the thermocapillary stresses, and the onset of convection.



## 7. Conclusions

As several recent experimental (Li & Yoda 2015) and numerical (Qin 2015) studies have demonstrated, phase change has a rather dramatic effect on the stability of the flow in a layer of a volatile liquid (0.65 cSt silicone oil) driven by a horizontal temperature gradients. These studies showed that the onset of convection is suppressed rather significantly when the phase change is enhanced by removing noncondensable gases, such as air, from the system. Linear stability analysis produces results that are overall in good quantitative agreement with these studies. In particular, it confirms that the instability that is responsible for generating a pattern of convection rolls is caused by the thermocapillary stresses, while buoyancy in the liquid layer has a stabilizing effect.

The analysis also shows that the magnitude of the effect is described by the nondimensional combination defined by (3.31), the same combination that appears in the convection problem with a vertical, rather than horizontal, temperature gradient (Chauvet *et al.* 2012). The similarity of the two problems is not coincidental: due to the weakness of advective fluxes, the effect of the gas phase is primarily described by diffusive transport of mass and heat, which is essentially the same in both cases.

Even when phase change is suppressed (e.g., at atmospheric conditions or for a fluid with relatively low volatility) we find that the gas phase can have a noticeable effect. Our analysis shows that the transport of heat in the gas layer can account for an increase of several percent in the critical Marangoni number. The effect of heat transport through the gas layer has been traditionally described using Newton cooling law, with the magnitude of the heat flux characterized by the Biot number. While this may be a reasonable approximation for the base flow, it breaks down completely the moment convection rolls appear. In fact, Newton cooling law fails to describe even the stability of the base flow and has to be abandoned in favour of a proper two-sided model to obtain quantitatively accurate results.

## Acknowledgements

This work was supported in part by the National Science Foundation under Grant No. CMMI-1511470.

## Appendix A. Numerical Solution of the Boundary Value Problem

The boundary value problems arising in the linear stability analysis were solved using the function `bvp5c` in Matlab 2013a. This function takes a system of first-order ODEs as input, so the higher-order ODEs were converted to this form.

### A.1. Diffusion-Dominated Case

For the diffusion dominated case, we converted the boundary value problem (4.16) to a system of six first-order ODEs

$$\begin{aligned} y_1' &= y_2, & y_2' &= y_3, \\ y_3' &= y_4, & y_4' &= C_4(\tilde{z})y_1 + C_5(\tilde{z})y_3 + iGrqy_5, \\ y_5' &= y_6, & y_6' &= C_6(\tilde{z})y_1 + Pr y_2 + C_7(\tilde{z})y_5, \end{aligned} \tag{A 1}$$

where  $y_1 = \tilde{\psi}_{lq}$ ,  $y_5 = \tilde{\theta}_{lq}$ , and

$$\begin{aligned} C_4(\tilde{z}) &= -i Gr \frac{q^3(\tilde{z}+1)(8\tilde{z}^2+\tilde{z}-1)}{48} - i Gr q \frac{8\tilde{z}+3}{8} \\ &\quad + i Re \frac{q^3(\tilde{z}+1)(3\tilde{z}+1)+6q}{4} - q^2(q^2+\sigma_q), \\ C_5(\tilde{z}) &= i Gr \frac{q(\tilde{z}+1)(8\tilde{z}^2+\tilde{z}-1)}{48} - i Re \frac{q(\tilde{z}+1)(3\tilde{z}+1)}{4} + 2q^2 + \sigma_q, \\ C_6(\tilde{z}) &= i Ma Pr q C_3(\tilde{z}), \\ C_7(\tilde{z}) &= -i Ma q C_1(\tilde{z}) + \sigma_q Pr + q^2. \end{aligned} \quad (\text{A } 2)$$

Respectively, the boundary conditions become

$$\begin{aligned} y_1(-1) &= 0, & y_1(0) &= 0, \\ y_2(-1) &= 0, & y_6(-1) &= 0, \\ y_3(0) + iq Re y_5(0) &= 0 \end{aligned} \quad (\text{A } 3)$$

and

$$y_6(0) + Bi_q y_5(0) = 0. \quad (\text{A } 4)$$

#### A.2. Transient Dynamics in the Gas Layer

To avoid solving coupled boundary value problems (4.16) and (4.24) defined on adjacent domains, we remapped the domain of  $\tilde{\theta}_{gq}$  and  $\tilde{\zeta}_{vq}$  from  $[0, A]$  to  $[-1, 0]$  by defining  $\bar{z} = -\tilde{z}/A$  and introducing two new functions  $\bar{\theta}_{gq}(\bar{z}) = \tilde{\theta}_{gq}(-\tilde{z})$  and  $\bar{\zeta}_{vq}(\bar{z}) = \tilde{\zeta}_{vq}(-\tilde{z})$ . In terms of these new functions, equations (4.22) become

$$\begin{aligned} A^{-2} \bar{\theta}_{gq}'' - q^2 \bar{\theta}_{gq} &= \sigma_q K_\alpha^{-1} \bar{\theta}_{gq}, \\ A^{-2} \bar{\zeta}_{vq}'' - q^2 \bar{\zeta}_{vq} &= \sigma_q K_D^{-1} \bar{\zeta}_{vq}, \end{aligned} \quad (\text{A } 5)$$

where the prime now denotes the derivative with respect to  $\bar{z}$ ,

The boundary condition (4.23) is replaced with

$$A \tilde{\theta}_{lq}'(0) = -\frac{k_g}{k_l} \bar{\theta}_{gq}'(0) - \frac{1-c_a^0}{c_a^0} H \bar{\zeta}_{vq}'(0), \quad (\text{A } 6)$$

Furthermore, the no-flux boundary conditions at the top of the gas layer become

$$\begin{aligned} \bar{\theta}_{gq}'(-1) &= 0, \\ \bar{\zeta}_{vq}'(-1) &= 0. \end{aligned} \quad (\text{A } 7)$$

Temperature continuity and the local phase equilibrium (4.11) at the free surface yield

$$\begin{aligned} \bar{\theta}_{gq}(0) &= \tilde{\theta}_{lq}(0), \\ \bar{\zeta}_{vq}(0) &= \tilde{\theta}_{gq}(0). \end{aligned} \quad (\text{A } 8)$$

Converting (A 5) into a system of first-order ODEs yields four additional equations

$$\begin{aligned} y_7' &= y_8, & y_8' &= A^2(q^2 + K_\alpha^{-1}\sigma_q)y_7, \\ y_9' &= y_{10}, & y_{10}' &= A^2(q^2 + K_D^{-1}\sigma_q)y_9, \end{aligned} \quad (\text{A } 9)$$

where  $y_7 = \bar{\theta}_{gq}$ , and  $y_9 = \bar{\zeta}_{vq}$ , which should be added to the system (A 1). The boundary

conditions (A 3) remain and (A 4) is replaced with

$$\begin{aligned} Ay_6(0) + \frac{k_g}{k_l}y_8(0) + \frac{1 - c_a^0}{c_a^0}Hy_{10}(0) &= 0, \\ y_7(0) &= y_5(0), \quad y_8(-1) = 0, \\ y_9(0) &= y_5(0), \quad y_{10}(-1) = 0. \end{aligned} \quad (\text{A } 10)$$

### A.3. The Effect of Advection in the Gas Layer

Just like in the previous case, we introduce new functions  $\bar{\theta}_{gq}(\bar{z}) = \tilde{\theta}_{gq}(-\bar{z})$ ,  $\bar{\varsigma}_{vq}(\bar{z}) = \bar{\varsigma}_{vq}(-\bar{z})$ , and  $\bar{\psi}_{gq}(\bar{z}) = \tilde{\psi}_{gq}(-\bar{z})$ , so (4.24) becomes

$$\begin{aligned} \bar{\nabla}_q^2 \bar{\nabla}_q^2 \bar{\psi}_{gq} + iq\bar{C}_1(\bar{z})\mathcal{R}A^{-2}\bar{\psi}_{gq}'' - iq\bar{C}_2(\bar{z})\mathcal{R}\bar{\psi}_{gq} - iq\Xi_T\bar{\theta}_{gq} - iq\Xi_\varsigma\bar{\varsigma}_{vq} &= \sigma_q\bar{\nabla}_q^2\bar{\psi}_{gq}, \\ K_\alpha\bar{\nabla}_q^2\bar{\theta}_{gq} + iq\bar{C}_1(\bar{z})\mathcal{R}\bar{\theta}_{gq} - iq\bar{C}_3(\bar{z})\mathcal{R}K_\alpha^{-1}\bar{\psi}_{gq} + A^{-1}\bar{\psi}_{gq}' &= \sigma_q\bar{\theta}_{gq}, \\ K_D\bar{\nabla}_q^2\bar{\varsigma}_{vq} + iq\bar{C}_1(\bar{z})\mathcal{R}\bar{\varsigma}_{vq} - iq\bar{C}_3(\bar{z})\mathcal{R}K_D^{-1}\bar{\psi}_{gq} + A^{-1}\bar{\psi}_{gq}' &= \sigma_q\bar{\varsigma}_{vq}. \end{aligned} \quad (\text{A } 11)$$

where we have defined  $\bar{\nabla}_q^2 = A^{-2}\partial_{\bar{z}}^2 - q^2$  and

$$\begin{aligned} \bar{C}_1(\bar{z}) &= \frac{(\bar{z}+1)(3\bar{z}+1)}{4} - \mathcal{B}\frac{(\bar{z}+1)(8\bar{z}^2+\bar{z}-1)}{48}, \\ \bar{C}_2(\bar{z}) &= q^2\bar{C}_1(\bar{z}) + \frac{3}{2A^2} - \mathcal{B}\frac{8\bar{z}+3}{8A^2}, \\ \bar{C}_3(\bar{z}) &= -\frac{A\bar{z}(\bar{z}+1)^2}{4} + \mathcal{B}\frac{A\bar{z}(\bar{z}+1)^2(2\bar{z}-1)}{48}. \end{aligned} \quad (\text{A } 12)$$

The functions  $\bar{\varsigma}_{vq}(\bar{z})$  and  $\bar{\theta}_{gq}(\bar{z})$  again satisfy the boundary conditions (A 7) and (A 8). The boundary conditions for the function  $\bar{\psi}_{gq}(\bar{z})$  follow from (3.21) and (3.22):

$$\begin{aligned} \bar{\psi}_{gq}(-1) &= 0, \quad \bar{\psi}_{gq}'(-1) = 0 \\ \bar{\psi}_{gq}(0) &= 0, \quad \bar{\psi}_{gq}'(0) = -A\bar{\psi}_{lq}'(0). \end{aligned} \quad (\text{A } 13)$$

Converting (A 11) into a system of first-order ODEs yields eight additional equations

$$\begin{aligned} y_7' &= y_8, \quad y_8' = \bar{C}_4(\bar{z})y_7 + iqA^2\mathcal{R}K_\alpha^{-2}\bar{C}_3(\bar{z})y_{11} - AK_\alpha^{-1}y_{12}, \\ y_9' &= y_{10}, \quad y_{10}' = \bar{C}_5(\bar{z})y_9 + iqA^2\mathcal{R}K_D^{-2}\bar{C}_3(\bar{z})y_{11} - AK_D^{-1}y_{12}, \\ y_{11}' &= y_{12}, \quad y_{12}' = y_{13}, \\ y_{13}' &= y_{14}, \quad y_{14}' = iqA^4K_\nu^{-1}(\Xi_Ty_7 + \Xi_\varsigma y_9) + \bar{C}_6y_{11} + \bar{C}_7y_{13}, \end{aligned} \quad (\text{A } 14)$$

which augment the system (A 1) describing the liquid layer. Here  $y_7 = \bar{\theta}_{gq}$ ,  $y_9 = \bar{\varsigma}_{vq}$ ,  $y_{11} = \bar{\psi}_{gq}$ , and

$$\begin{aligned} \bar{C}_4(\bar{z}) &= -iqA^2\mathcal{R}K_\alpha^{-1}\bar{C}_1(\bar{z}) + A^2(q^2 + K_\alpha^{-1}\sigma_q), \\ \bar{C}_5(\bar{z}) &= -iqA^2\mathcal{R}K_D^{-1}\bar{C}_1(\bar{z}) + A^2(q^2 + K_D^{-1}\sigma_q), \\ \bar{C}_6(\bar{z}) &= iqA^4\mathcal{R}K_\nu^{-1}\bar{C}_2(\bar{z}) - A^4q^2(q^2 + K_\nu^{-1}\sigma_q), \\ \bar{C}_7(\bar{z}) &= -iqA^2\mathcal{R}K_\nu^{-1}\bar{C}_1(\bar{z}) + A^2(2q^2 + K_\nu^{-1}\sigma_q). \end{aligned} \quad (\text{A } 15)$$

The boundary conditions are given by (A 3), (A 10), and

$$\begin{aligned} y_{11}(0) &= 0, \quad y_{11}(-1) = 0, \\ y_{12}(0) &= -Ay_2(0), \quad y_{12}(-1) = 0. \end{aligned} \quad (\text{A } 16)$$

In all of the expressions given in the Appendix, the nondimensional parameters  $Re$ ,  $Gr$ ,  $\mathcal{R}$ ,  $\mathcal{B}$ ,  $\Xi_T$ , and  $\Xi_\varsigma$  were expressed in terms of  $Ma$ ,  $Pr$ ,  $Bo_D$ , and  $c_a^0$  using the definitions

(3.3), (3.5), (3.7), (3.15), (3.30), (3.39), and (3.40). Similarly, parameters  $K_D$ ,  $K_\alpha$  and  $K_\nu$  were evaluated as functions of  $c_a^0$ .

## REFERENCES

- BEN HADID, H. & ROUX, B. 1992 Buoyancy- and thermocapillary-driven flows in differentially heated cavities for low-prandtl-number fluids. *J. Fluid Mech.* **235**, 1–36.
- BIRIKH, R. V. 1966 Thermocapillary convection in a horizontal layer of liquid. *J. Appl. Mech. Tech. Phys.* **7**, 43–44.
- BURELBACH, J. P., BANKOFF, S. G. & DAVIS, S. H. 1988 Nonlinear stability of evaporating/condensing liquid films. *J. Fluid Mech.* **195**, 463–494.
- BURGUETE, J., MUKOLOBWIEZ, N., DAVIAUD, F., GARNIER, N. & CHIFFAUDEL, A. 2001 Buoyant-thermocapillary instabilities in extended liquid layers subjected to a horizontal temperature gradient. *Phys. Fluids* **13** (10), 2773–2787.
- CHAN, CHO LIK. & CHEN, C. F. 2010 Effect of gravity on the stability of thermocapillary convection in a horizontal fluid layer. *J. Fluid Mech.* **647**, 91–103.
- CHAUVET, F., DEHAECK, S. & COLINET, P. 2012 Threshold of benard-marangoni instability in drying liquid films. *Epl* **99** (3).
- CROSS, M. C. & GREENSIDE, H. 2009 *Pattern Formation and Dynamics in Nonequilibrium Systems*. Cambridge: Cambridge University Press.
- DE SAEDELEER, C., GARCIMARTÍN, A., CHAVEPEYER, G., PLATTEN, J. K. & LEBON, G. 1996 The instability of a liquid layer heated from the side when the upper surface is open to air. *Phys. Fluids* **8** (3), 670–676.
- GARCIMARTÍN, ANGEL, MUKOLOBWIEZ, NATHALIE & DAVIAUD, FRANÇOIS 1997 Origin of waves in surface-tension-driven convection. *Phys. Rev. E* **56**, 1699–1705.
- HA, J. M. & PETERSON, G. P. 1994 Analytical prediction of the axial dryout point for evaporating liquids in triangular microgrooves. *ASME J. Heat Transfer* **116**, 498–503.
- Ji, Y., LIU, Q.-S. & LIU, R. 2008 Coupling of evaporation and thermocapillary convection in a liquid layer with mass and heat exchanging interface. *Chin. Phys. Lett.* **25**, 608–611.
- KAVEHPUR, PIROUZ, OVRYN, BEN & MCKINLEY, GARETH H. 2002 Evaporatively-driven marangoni instabilities of volatile liquid films spreading on thermally conductive substrates. *Colloids and Surfaces A: Physicochemical and Engineering Aspects* **206** (13), 409 – 423.
- KIRDYASHKIN, A. G. 1984 Thermogravitational and thermocapillary flows in a horizontal liquid layer under the conditions of a horizontal temperature gradient. *Int. J. Heat Mass Transfer* **27**, 1205–1218.
- KLENTZMAN, J. & AJAEV, V. S. 2009 The effect of evaporation on fingering instabilities. *Phys. Fluids* **21**, 122101.
- LI, Y., GRIGORIEV, R. O. & YODA, M. 2014 Experimental study of the effect of noncondensables on buoyancy-thermocapillary convection in a volatile low-viscosity silicone oil. *Phys. Fluids* **26**, 122112.
- LI, Y. & YODA, M. 2015 The wave length of the pattern for buoyancy-thermocapillary convection in 0.65 cSt silicone oil. Private communication.
- LI, YOU-RONG, ZHANG, HONG-RU, WU, CHUN-MEI & XU, JIN-LIANG 2012 Effect of vertical heat transfer on thermocapillary convection in an open shallow rectangular cavity. *Heat Mass Transfer* **48**, 241–251.
- LU, X. & ZHUANG, L. 1998 Numerical study of buoyancy- and thermocapillary-driven flows in a cavity. *Acta Mech Sinica (English Series)* **14** (2), 130–138.
- MARKOS, M., AJAEV, V. S. & HOMSY, G. M. 2006 Steady flow and evaporation of a volatile liquid in a wedge. *Phys. Fluids* **18**, 092102.
- MERCIER, J. & NORMAND, C. 2002 Influence of the prandtl number on the location of recirculation eddies in thermocapillary flows. *Int. J. Heat Mass Transfer* **45**, 793–801.
- MERCIER, J. F. & NORMAND, C. 1996 Buoyant-thermocapillary instabilities of differentially heated liquid layers. *Phys. Fluids* **8**, 1433–1445.
- MUNDRANE, M. & ZEBIB, A. 1994 Oscillatory buoyant thermocapillary flow. *Phys. Fluids* **6** (10), 3294–3306.

- NORMAND, C., POMEAU, Y. & VELARDE, M. 1977 Convective instability: A physicist's approach. *Rev. Modern Phys.* **49**, 581.
- PARMENTIER, P. M., REGNIER, V. C. & LEBON, G. 1993 Buoyant-thermocapillary instabilities in medium-prandtl-number fluid layers subject to a horizontal gradient. *Int. J. Heat Mass Transfer* **36**, 2417–2427.
- PRIEDE, J. & GERBETH, G. 1997 Convective, absolute, and global instabilities of thermocapillary-buoyancy convection in extended layers. *Phys. Rev. E* **56** (4), 4187–4199.
- QIN, T. & GRIGORIEV, R. O. 2015 The effect of noncondensables on buoyancy-thermocapillary convection of volatile fluids in confined geometries. *Int. J. Heat Mass Transf.* **90**, 678–688.
- QIN, T., Ž. TUKOVIĆ & GRIGORIEV, R. O. 2014 Buoyancy-thermocapillary convection of volatile fluids under atmospheric conditions. *Int. J. Heat Mass Transf.* **75**, 284–301.
- QIN, T., Ž. TUKOVIĆ & GRIGORIEV, R. O. 2015 Buoyancy-thermocapillary convection of volatile fluids under their vapors. *Int. J. Heat Mass Transf.* **80**, 38–49.
- RILEY, R. J. & NEITZEL, G. P. 1998 Instability of thermocapillarybuoyancy convection in shallow layers. Part 1. Characterization of steady and oscillatory instabilities. *J. Fluid Mech.* **359**, 143–164.
- SCHATZ, M. F. & NEITZEL, G. P. 2001 Experiments on thermocapillary instabilities. *Annu. Rev. Fluid Mech.* **33**, 93–127.
- SCHRAGE, R. W. 1953 *A Theoretical Study of Interface Mass Transfer*. New York: Columbia University Press.
- SHEVTSOVA, V. M. & LEGROS, J. C. 2003 Instability in thin layer of liquid confined between rigid walls at different temperatures. *Acta Astronautica* **52** (7), 541–549.
- SHEVTSOVA, V. M., NEPOMNYASHCHY, A. A. & LEGROS, J. C. 2003 Thermocapillary-buoyancy convection in a shallow cavity heated from the side. *Phys. Rev. E* **67**, 066308.
- SMITH, MARC K. & DAVIS, STEPHEN H. 1983*a* Instabilities of dynamic thermocapillary liquid layers. part 1. convective instabilities. *J. Fluid Mech.* **132**, 119–144.
- SMITH, MARC K. & DAVIS, STEPHEN H. 1983*b* Instabilities of dynamic thermocapillary liquid layers. part 2. surface-wave instabilities. *J. Fluid Mech.* **132**, 145–162.
- SUMAN, B. & KUMAR, P. 2005 An analytical model for fluid flow and heat transfer in a micro-heat pipe of polygonal shape. *International Journal of Heat and Mass Transfer* **48** (21-22), 4498–4509.
- VILLERS, D. & PLATTEN, J. K. 1987 Separation of marangoni convection from gravitational convection in earth experiments. *Phys. Chem. Hydrodyn.* **8**, 173–183.
- VILLERS, D. & PLATTEN, J. K. 1992 Coupled buoyancy and marangoni convection in acetone: experiments and comparison with numerical simulations. *J. Fluid Mech.* **234**, 487–510.
- YAWS, CARL L. 2003 *Yaws' Handbook of Thermodynamic and Physical Properties of Chemical Compounds (Electronic Edition): physical, thermodynamic and transport properties for 5,000 organic chemical compounds*. Norwich: Knovel.
- YAWS, CARL L. 2009 *Yaws' Thermophysical Properties of Chemicals and Hydrocarbons (Electronic Edition)*. Norwich: Knovel.